iScience

CellPress

Article

Deacetylation Inhibition Reverses PABPN1-Dependent Muscle Wasting

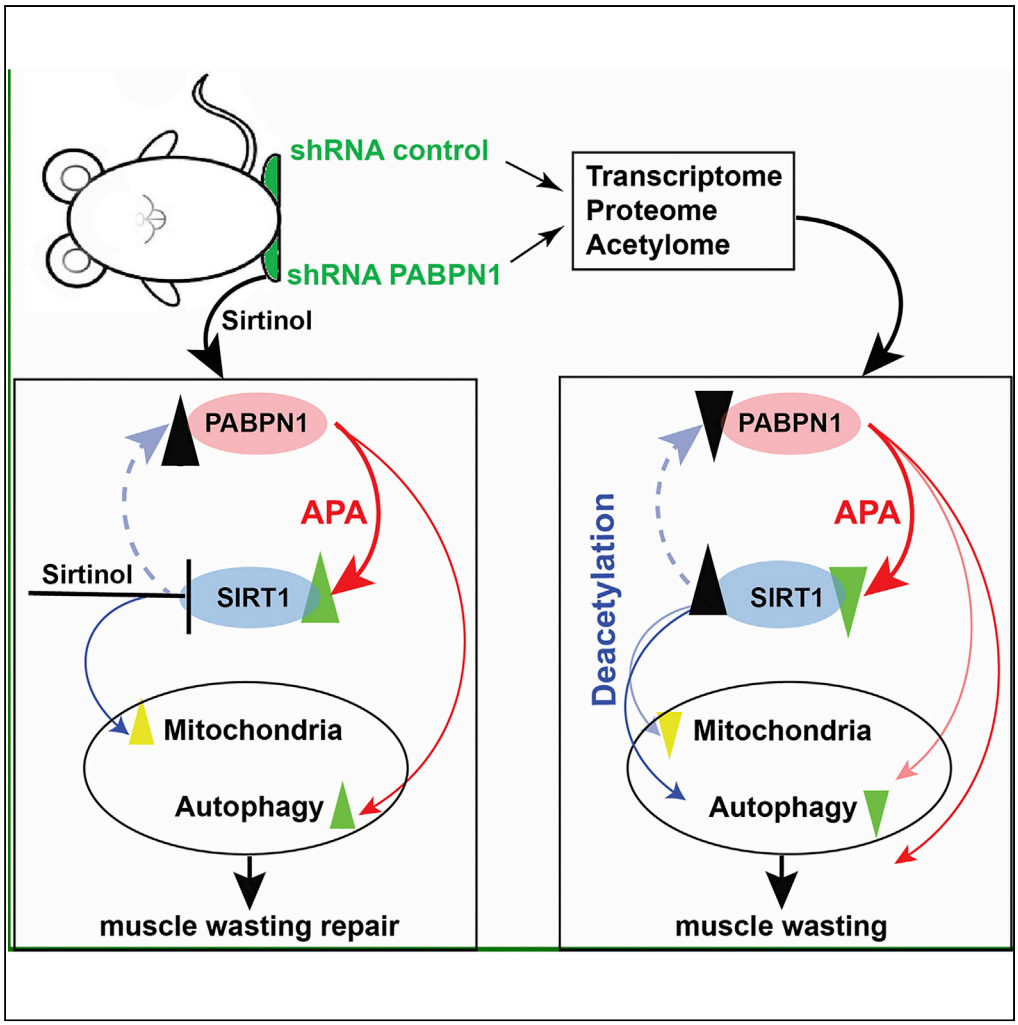

Cyriel S. Olie, Muhammad Riaz, Rebecca Konietzny, ..., Jelle J. Goeman, Benedikt M. Kessler, Vered Raz

v.raz@lumc.nl

HIGHLIGHTS

The PABPN1 transcriptome has smaller changes than its corresponding proteome

The PABPN1 proteome is marked by protein deacetylation and elevated SIRT1 deacetylase

SIRT1 levels are controlled by PABPN1 via alternative polyadenylation utilization

Deacetylation inhibition reversed hallmark of muscle wasting in shPab muscles

Olie et al., iScience *12*, 318–332
February 22, 2019
https://doi.org/10.1016/j.isci.2019.01.024

iScience

CellPress

Article

Deacetylation Inhibition Reverses PABPN1-Dependent Muscle Wasting

Cyriel S. Olie,[1] Muhammad Riaz,[1] Rebecca Konietzny,[2] Philip D. Charles,[2] Adan Pinto-Fernandez,[2] Szymon M. Kiełbasa,[3] A. Aartsma-Rus,[1] Jelle J. Goeman,[3] Benedikt M. Kessler,[2,4] and Vered Raz[1,4,5,*]

SUMMARY

Reduced poly(A)-binding protein nuclear 1 (PABPN1) levels cause aging-associated muscle wasting. PABPN1 is a multifunctional regulator of mRNA processing. To elucidate the molecular mechanisms causing PABPN1-mediated muscle wasting, we compared the transcriptome with the proteome in mouse muscles expressing short hairpin RNA to PABPN1 (shPab). We found greater variations in the proteome than in mRNA expression profiles. Protein accumulation in the shPab proteome was concomitant with reduced proteasomal activity. Notably, protein acetylation appeared to be decreased in shPab versus control proteomes (63%). Acetylome profiling in shPab muscles revealed prominent peptide deacetylation associated with elevated sirtuin-1 (SIRT1) deacetylase. We show that SIRT1 mRNA levels are controlled by PABPN1 via alternative polyadenylation site utilization. Most importantly, SIRT1 deacetylase inhibition by sirtinol increased PABPN1 levels and reversed muscle wasting. We suggest that perturbation of a multifactorial regulatory loop involving PABPN1 and SIRT1 plays an imperative role in aging-associated muscle wasting.

INTRODUCTION

Muscle wasting is prominent in many pathologies including metabolic disorders and neuromuscular diseases. Muscle wasting is also associated with aging and is highly prevalent in the elderly (Bowen et al., 2015). The molecular and cellular causes for aging-associated muscle wasting are diverse. Recently, we reported that muscle wasting is induced by reduced levels of poly(A)-binding protein nuclear 1 (PABPN1) (Riaz et al., 2016). PABPN1 levels are normally reduced in skeletal muscles during aging and are also associated with muscle weakness in oculopharyngeal muscular dystrophy (OPMD), a late-onset myopathy (Anvar et al., 2013). An expansion mutation in PABPN1 is the genetic cause for OPMD (Brais et al., 1998). In OPMD, PABPN1 aggregates and hence depletes the levels of the functional protein (Raz et al., 2011). PABPN1 regulates poly(A) tail length, alternative polyadenylation (APA) in the 3′ UTR or in internal regions, and nuclear export of transcripts, which together will affect mRNA expression levels, leading to an altered transcriptome (Banerjee et al., 2013). The mechanisms by which PABPN1 depletion leads to muscle wasting are not fully understood.

Muscle wasting in OPMD mouse models is associated with the ubiquitin proteasome system (UPS) (Anvar et al., 2011a, 2011b; Trollet et al., 2010). Also, in the mouse muscles with PABPN1 knockdown (shPab) muscle atrophy was found to be associated with altered mRNA levels of UPS genes that regulate muscle atrophy (Riaz et al., 2016). Reduced proteasomal activity in shPab muscles suggests that protein homeostasis is altered in shPab muscles. Protein homeostasis plays a central role in aging-associated muscle wasting (Cohen et al., 2014). Muscle contraction demands mitochondrial activity, and unsurprisingly altered mitochondrial activity was found in OPMD models, which was concomitant with shortened poly(A) tail length and APA in the 3′ UTR of mitochondrial genes (Chartier et al., 2015; Vest et al., 2017). Yet, how altered mRNA expression profiles lead to muscle wasting remains obscure.

Here we applied RNA sequencing (RNA-seq) and mass spectrometry in shPab muscles to identify the molecular and cellular causes for muscle wasting. We show that protein acetylation is reduced in shPab muscles and that deacetylation inhibition restores PABPN1-mediated muscle wasting.

RESULTS

PABPN1 Down-regulation Alters Muscle Histology

We investigated the molecular mechanisms that are associated with PABPN1-driven muscle wasting in mouse tibialis anterior muscles expressing short hairpin RNA (shRNA) to *Pabpn1* (shPab). PABPN1 levels

[1]Department of Human Genetics, Leiden University Medical Center, Leiden, The Netherlands

[2]Target Discovery Institute, Nuffield Department of Medicine, University of Oxford, Oxford OX3 7FZ, UK

[3]Medical Statistics and Bioinformatics, Leiden University Medical Center, Leiden, The Netherlands

[4]These authors contributed equally

[5]Lead Contact

*Correspondence: v.raz@lumc.nl

https://doi.org/10.1016/j.isci.2019.01.024

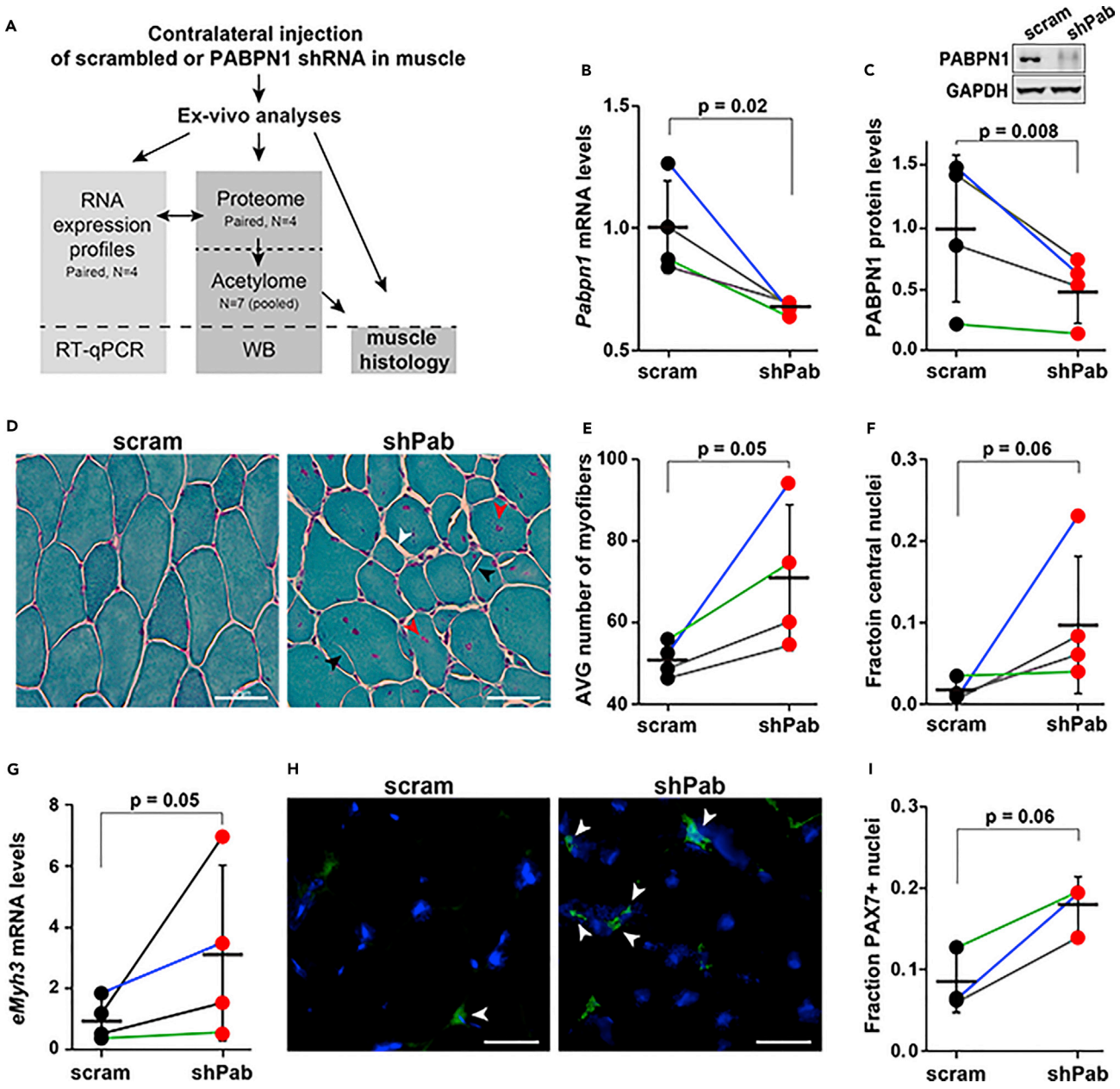

Figure 1. Reduced PABPN1 Levels Induce Muscle Regeneration

(A) Schematic workflow of the *ex vivo* analyses in scram and shPab muscles. RNA expression profiles (RNA-seq) are compared with the shPab proteome of the same muscles. The shPab acetylome was then analyzed. Procedures were validated using qRT-PCR, western blot (WB), or muscle histology. *Ex vivo* experiments were performed on paired muscles (N = 4 mice).

(B) qRT-PCR of *Pabpn1* mRNA levels after normalization to Hprt housekeeping control. Paired dot plot is from N = 4 mice.

(C) PABPN1 protein and levels in paired muscles. Representative western blot of PABPN1 and GAPDH loading control are shown. Paired dot plot shows PABPN1 levels after normalization to loading control, N = 4 mice.

(D) Gomori trichrome tissue histology in cross sections. Images are of the mouse with highest PABPN1 fold change. White arrowheads point to ECM thickening, central myonuclei are depicted with red arrowheads, and split myofibers with black arrowheads. Scale bar, 50 μm.

(E) Paired dot plot shows the mean number of myofibers per image frame, calculated from 5 frames per muscle (N = 8 muscles).

(F) Paired dot plot shows the mean fraction of central nuclei in myofibers, calculated from 5 frames per muscle (N = 8 muscles).

(G) Paired dot plot shows *eMyh3* mRNA levels in scram and shPab muscles (N = 4 mice). Expression values were calculated after normalization to *Hprt* and to the average *eMyh3* expression of all scram muscles.

Figure 1. *Continued*

(H and I) (H) Representative fluorescent images for scram and shPab muscles stained with PAX7 antibody (green). Nuclei are counterstained with DAPI (blue). White arrowheads indicate nuclear PAX7. Scale bar, 7.5μm. (I) Paired dot plot shows the fraction of PAX7 positive nuclei in paired muscles. The percentage was calculated from over 1,000 nuclei per muscle (N = 6 muscles). In all dot plots paired muscles are connected with lines; blue or green lines mark the mouse with the highest or lowest PABPN1 fold change, respectively. Quantification of the muscle histology was performed over the entire muscle cross section. Means and standard deviations are depicted. Statistical difference was assessed with a paired test.

in muscles from four mice were compared between shPab and scrambled shRNA (scram) after contralateral injection, as previously described (Riaz et al., 2016). In this experimental setup analysis was paired, overcoming natural variations between mice. Muscles were harvested for *ex vivo* procedures including RNA-seq and mass spectrometry, and validations were carried out using qRT-PCR, western blot, and muscle histology (Figure 1A). Transduction efficiency was assessed by GFP fluorescence, which was included in the expression cassette. Overall, similar fluorescence was found in shPab and scram muscles (Figure S1), indicating that any alterations in PABPN1 levels are not due to variation in transduction efficiency. Analysis of PABPN1 demonstrated reduced levels in shPab muscles (Figures 1B and 1C). Muscle histology was found to be altered between scram and shPab (Figure 1D). We confirmed thickening of the extracellular matrix (ECM) in shPab muscles (Figure 1D; Riaz et al., 2016). We also measured more myofibers per image frame in shPab compared with scram muscles (Figure 1E). Smaller myofibers could result from muscle atrophy, which is consistent with our previous study (Riaz et al., 2016); furthermore, it can concur with muscle regeneration. Central myonuclei and split myofibers were found in shPab muscles (Figure 1D). The fraction of central myonuclei in shPab was higher in three of the four mice (Figure 1F). PAX7 and *eMyh3* expression are molecular signatures of muscle regeneration (Lepper et al., 2011; Sambasivan et al., 2011; Schiaffino et al., 2015). qRT-PCR of *eMyh3* mRNA revealed higher levels in shPab muscles (Figure 1G). PAX7 staining also showed the same trend, wherein the fraction of PAX7-positive myonuclei was higher in shPab muscles (Figures 1H and 1I). Noticeably, the mouse with the highest PABPN1 fold change showed the most severe histological changes, whereas the mouse with the lowest fold change showed resilient changes.

Proteomic Changes Surpass the Transcriptomic Changes in shPab Muscles

The molecular mechanisms that are associated with PABPN1-mediated muscle pathology were investigated in the shPab transcriptome and proteome from the same muscles, using paired ratio t test. The shPab RNA expression profiles included 363 genes (5% false discovery rate [FDR]; Figure 2A, related to Table S1), and those were predominantly enriched with genes of the ECM, mitochondria, and muscle-related genes (related to Table S2). These expression profiles are consistent with OPMD expression profiles (Anvar et al., 2011a; Raz et al., 2013). Moreover, higher expression of ECM genes is consistent with ECM thickening in shPab muscles (Riaz et al., 2016). qRT-PCR validation was carried out for *Pabpn1* and *eMyh3* (Figures 1 and 2A). For the proteome, a 5% FDR cutoff was too strict (Related to Table S3). Considering a p value cutoff of $p < 0.05$, we identified differential expression of additional genes, such as *Rad32a* and *Map1lc3a*, which were previously reported as differentially expressed in shPab (Raz et al., 2017; Riaz et al., 2016). The shPab proteome contained 248 differentially expressed proteins ($p < 0.05$) (Figure 2B, related to Table S3). Western blot for seven proteins validated the proteomics results (Figure S2). A significant correlation ($p = 2.2 \times 10^{-16}$) was found between mRNA and protein fold changes. The regression line is similar to the diagonal, although the correlation was small ($R = 0.31$) (Figure 2C). Overall, protein fold change was greater compared with mRNA fold change (Figure S3). Focusing on the group of genes or proteins with higher fold changes (average fold change > |1.5|) we found that the majority of the proteins had a positive fold change in shPab muscles (68%, Figure 2D). In contrast, a fold change direction preference was not found for the mRNAs (Figure 2D). The same fold change direction between mRNA and proteins was found for nearly 70% of the proteins, of which most proteins (74%) have higher levels in shPab (Figure 2E). In the group with opposite fold change direction between mRNA and protein (30%), the majority of proteins (80%) had higher levels in shPab (Figure 2E). Together, this suggests that in shPab muscles protein accumulation surpasses mRNA alterations. Moreover, protein accumulation in shPab suggests higher protein steady state, which is in agreement with reduced proteasome activity in shPab (Riaz et al., 2016).

A heatmap of the differential expressed proteins ($p < 0.05$, $N = 248$ proteins) across the four individual mice revealed that the largest differences between scram and shPab muscles were found in the mouse with the highest PABPN1 fold change, whereas in the mouse with the lowest PABPN1 fold change the differences were the smallest (Figure 3A). This trend was then confirmed using k-means clustering. For 83 proteins, fold changes highly correlated with PABPN1 levels (Figure S4). Validation using western blot was demonstrated

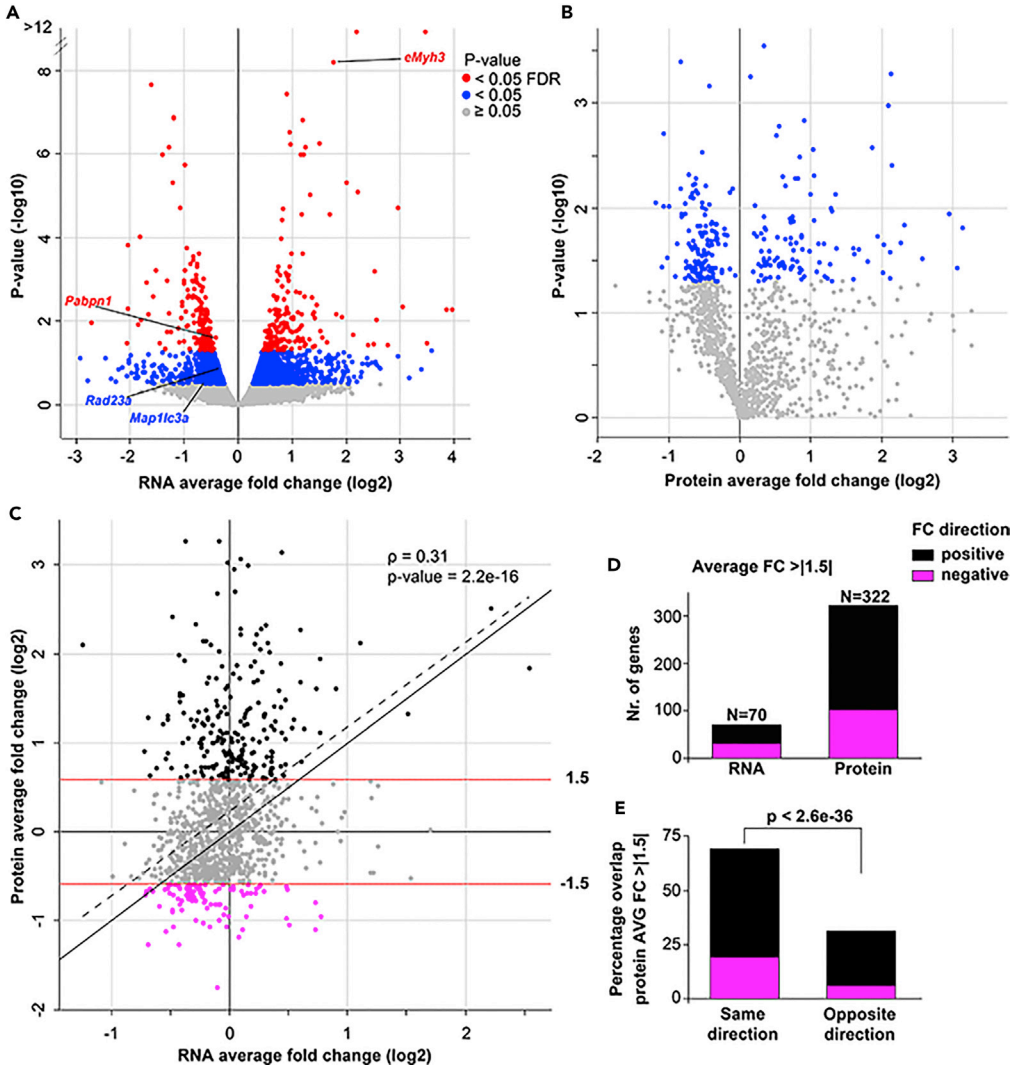

Figure 2. Reduced PABPN1 Levels Result in a Greater Effect on Proteome Compared with Transcriptome

(A) A volcano plot of the average mRNA fold change (FC) against p values in the shPab transcriptome. mRNAs that pass the cutoff p value < 0.05 or p values corrected for false discovery rate are depicted in blue or red, respectively. Examples of validated genes are highlighted.

(B) Volcano plot of the average protein fold change against p values in the shPab proteome. Proteins that pass the cutoff ($p < 0.05$) are depicted in blue.

(C) Scatterplot shows the fold changes between shPab proteome and transcriptome. Correlation (indicated as gray dashed line) was assessed with a Spearman rank test and compared with the diagonal (solid gray line). Average protein fold changes of 1.5 and −1.5 are indicated with red lines. Proteins with an average fold changes higher than 1.5 or lower than −1.5 are depicted in pink or black, respectively.

(D) Bar chart shows fold change direction of shPab-affected genes (average fold change cutoff > |1.5|) sorted for RNA or proteins.

(E) Bar chart shows the percentage of proteins (average fold change cutoff > |1.5|) with similar fold change direction or opposite fold change direction compared with RNA direction. Fold change higher than 1.5 is denoted in black and fold change lower than −1.5 in pink. Both transcriptome and proteome were determined from the same muscles (N = 4 mice).

for two proteins (Figure S2). Together, these results suggest that the levels of a subset of proteins strongly correlate with the PABPN1 fold change.

The cellular machineries that are affected by PABPN1 were then identified in the shPab proteome using enrichment analysis. The mitochondria, ribosome, cytoskeleton, nucleotide binding, glycolysis, and muscle

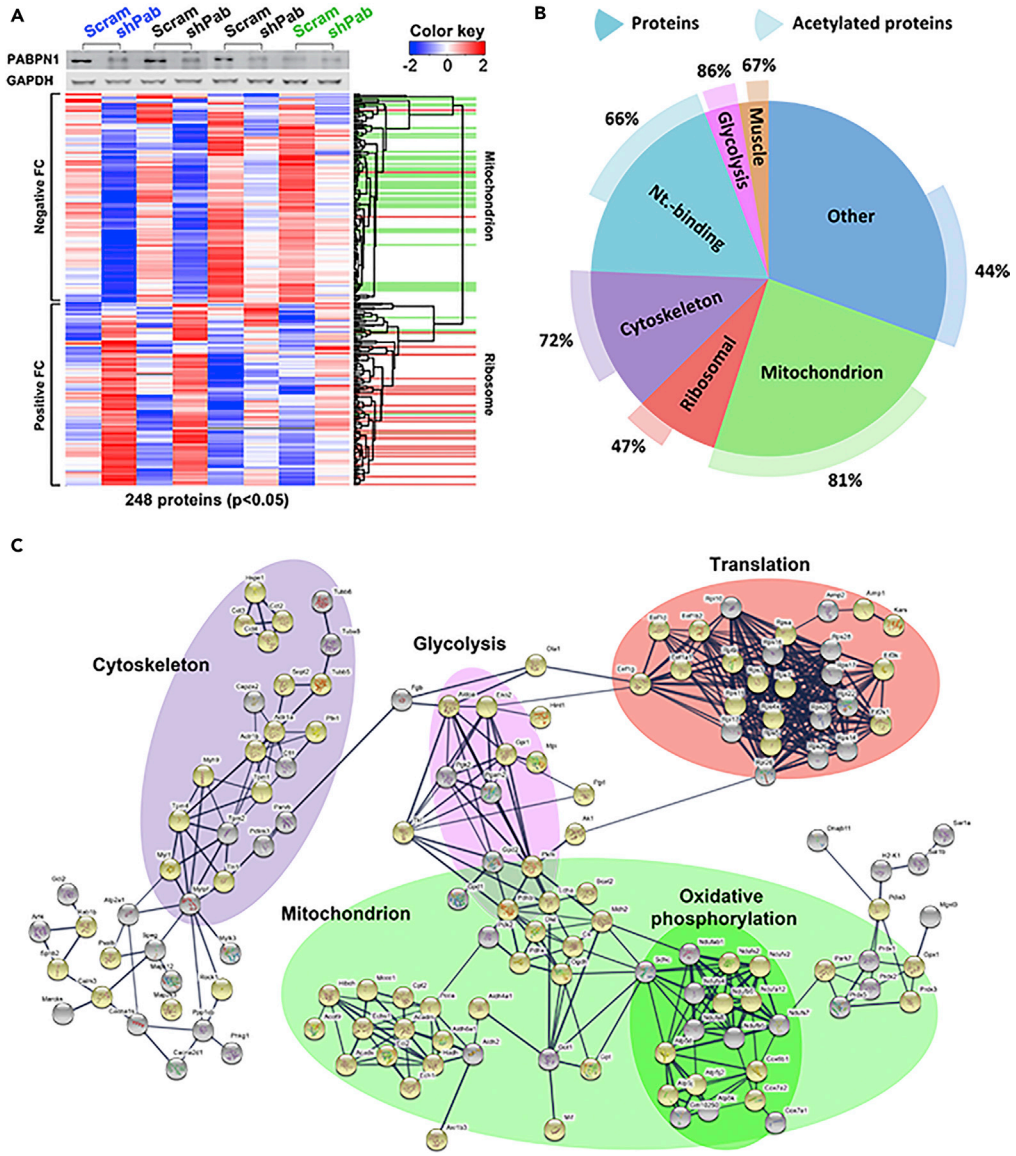

Figure 3. PABPN1 Levels Affect Muscle Proteome of Which a Large Part Is Linked to Acetylation

(A) Heatmap of protein abundance for the differentially expressed proteins ($p < 0.05$). Muscles are paired; the mice with the highest and lowest PABPN1 fold change are depicted in blue and green, respectively. Western blot shows PABPN1 expression for each mouse. GAPDH was used as loading control. Mitochondrial proteins are highlighted with green lines, and ribosomal proteins are highlighted with red lines. Color key indicates the *Z* scores (based on rows).

(B) Pie chart shows the significantly enriched protein groups (UP-keyword, David) of the differentially expressed proteins ($p < 0.05$, $n = 248$). The transparent pies (outer circle) indicate the number of proteins within the protein groups that are linked to protein acetylation group. Numbers indicate the percentage per group.

(C) The protein-protein interaction map shows protein networks for 248 proteins that pass the cutoff ($p < 0.05$). Mitochondrial (green), translation (red), cytoskeletal (purple), and glycolysis (pink) clusters are highlighted. Within the mitochondrial cluster, the oxidative phosphorylation group is highlighted in dark green. Unconnected proteins are not shown, and networks with $n < 4$ are removed. Proteins that are found in the acetylation group are highlighted in yellow, and those that were not found in the acetylation group are gray.

proteins were found to be the most prominently affected (Figure 3B). Notably, mitochondrial proteins had lower levels, whereas most of the ribosomal proteins had higher levels in shPab muscles (Figure 3A). Next, protein-protein interaction networks of the differentially expressed proteins revealed that networks of the mitochondria, translation, cytoskeleton, and glycolysis were the most connected (Figure 3C). This suggests

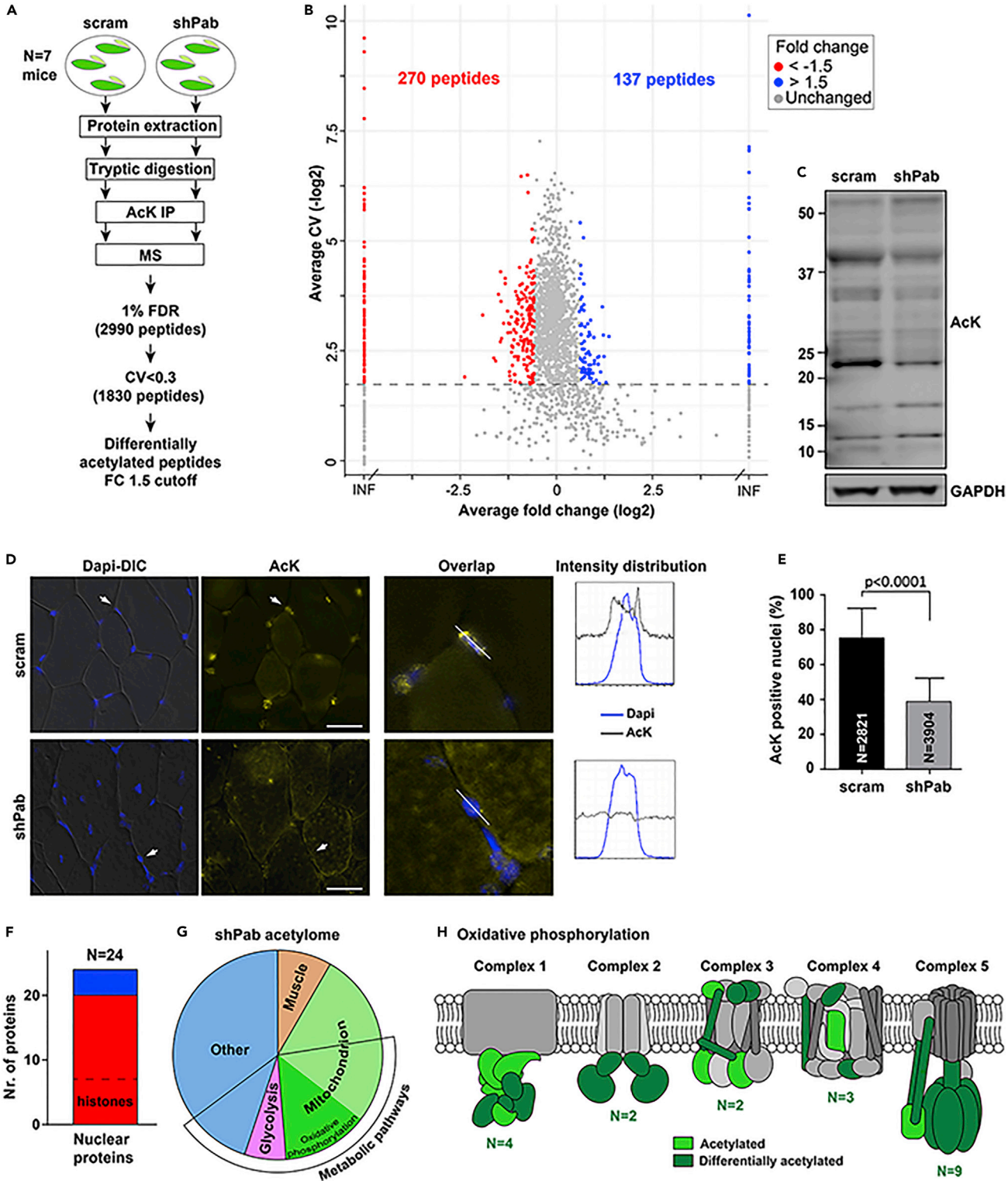

Figure 4. The shPab-Dependent Acetylome

(A) A workflow of the shPab acetylome procedure. Tibialis anterior muscles (N = 7 mice, contralateral injection of scram or shPab AAVs) were used. Protein extracts were pooled per genotype. Tryptic digestion, followed by immunoprecipitation with an anti-acetylated lysine (AcK) antibody, and mass spectrometry (MS) were carried out separately for the scram and shPab. Peptide analysis pipeline included an MS quality control (1% FDR) and coefficient of variation (CV) < 0.3. The differentially acetylated peptides were considered with a 1.5-fold change (fold change) cutoff.

Figure 4. *Continued*

(B) Scatterplot shows average peptide fold change (log2) versus average CV (-log2). Peptides with CV < 0.3 and a fold change of >1.5 and < -1.5 are depicted with blue and red, respectively. Peptides that are only found in either shPab or scram muscle are lined as INF (infinite). Unchanged peptides are depicted in gray. The dashed line marks CV < 0.3.

(C and D) (C) Western blot of acetylated proteins in scram and shPab muscle protein extracts. GAPDH is loading control. (D) Immunofluorescence with AcK antibody in scram and shPab muscle cryosections. Left panels show an overlay between bright-field and DAPI staining of the nuclei (blue). The middle panels show AcK signal (yellow). Right panels show an enlarged AcK and DAPI overlay around the nuclei that are marked with an arrow. Intensity distribution plots for DAPI and AcK signal are made from the nucleus, which is marked with a line. Examples of AcK-positive and AcK-negative nuclei are in the upper and lower plots, respectively. Scale bar, 5 μm.

(E) Bar chart shows the percentage of AcK-positive nuclei in scram and shPab muscles from four mice (unpaired). The number of measured nuclei is depicted within each bar. Trend for statistical difference was assessed with the Mann-Whitney test.

(F) Fold change direction of nuclear proteins in the shPab acetylome: positive and negative fold changes are depicted in blue and red, respectively.

(G) Pie chart shows the significantly affected gene ontology terms in the shPab acetylome.

(H) Schematic representation of the acetylated and the shPab differentially acetylated oxidative phosphorylation subunits. The acetylated subunits in tibialis anterior muscle are highlighted in light green, and the shPab differentially acetylated are in dark green. The number of affected proteins in each complex is depicted.

that the function of these cellular machineries is impaired in shPab muscles. Most striking, 63% of the proteins in the shPab proteome were enriched in the acetylation group (related to Table S4). Most mitochondrial proteins in the shPab proteome were also found in the acetylation group (Figures 3B and 3C). Moreover, acetylation was also found to be abundant in the other enriched cellular machineries (Figures 3B and 3C), suggesting that acetylation might have a prominent role in shPab muscles.

shPab Muscles Are Characterized by Reduced Protein Acetylation

To elucidate the acetylated protein landscape in shPab muscles, a peptide pull-down with an antibody to acetylate lysine was carried out in scram and shPab muscles. For this purpose, protein extracts from seven mice, which were injected contralaterally with scram or shPab adeno-associated virus (AAV) 9 particles, were pooled and the pull-down peptides were identified using mass spectrometry (Figure 4A). In total, 2,229 peptides passed the 1% FDR and overlapped between two independent runs (related to Table S5). A total of 1,830 peptides (82%) passed the coefficient of variation cutoff and were considered for subsequent analysis (Figure 4B). A confidence in the identified acetylated peptides was further assessed comparing our study in tibialis anterior muscles with the following published acetylome studies: in human and in rat skeletal muscles (Lundby et al., 2012) and in rat soleus (Ryder et al., 2015). Only ~13% of the acetylated peptides overlapped between the human and rodent acetylomes (related to Table S6A). As the human and rat studies came from the same laboratory and have a similar number of acetylated peptides (Lundby et al., 2012), it can be assumed that the limited overlap is not due to experimental settings or technical variations. The overlap between the two studies in rat was only 35% and comparable to the overlap between our study and the study in rat by Lundby et al. The specific muscle type was not specified in the study by Lundby et al. However, peptide overlap between fast-twitch tibialis anterior and slow-twitch soleus was only 13% (200 peptides; related to Table S6B). In the pool of the overlapping peptides between soleus and tibialis anterior the mitochondria was highly enriched (Table S6C), which is consistent with mitochondria enrichment in the acetylome studies in rat and humans (Lundby et al., 2012). Using western blot, we confirmed that the pattern of bulk protein acetylation highly differs between soleus and fast-twitch quadriceps in mouse (Figure S5). Differences in histone acetylation were reported between fast and slow muscles (Kawano et al., 2015). Moreover, 82% of those overlapping acetylated proteins are also annotated in DAVID as acetylated proteins (related to Table S6C). Together, this suggests that in skeletal muscles the acetylated mitochondrial proteins are highly abundant. Furthermore, it indicates that our acetylome study is suitable for further analysis.

We then investigated differential peptide acetylation between scram and shPab muscles and considered a fold change of 1.5 as a cutoff. In the shPab acetylome, 270 peptides were hypoacetylated and 137 peptides were hyperacetylated (Figure 4B). We found that 87 and 61 acetylated peptides were exclusively found in scram and shPab muscles, respectively (Figure 4B). This suggests an overall reduced acetylation in shPab muscles. Differences in protein acetylation between scram and shPab muscles were confirmed using western blot (Figure 4C). In addition, immunofluorescence also showed a decrease in the acetylation signal in shPab nuclei compared with scram muscles (Figures 4D and 4E). To confirm this observation, acetylation direction was assessed for nuclear proteins in the shPab acetylome. Hypoacetylation was also prominent in the nuclear proteins, including all histones (Figure 4F). Moreover, enrichment analysis of the differentially

acetylated proteins (N = 171) showed that the mitochondria was highly enriched (Figure 4G). In addition, 42% of the differentially acetylated proteins were enriched in metabolic pathways (Figure 4G). The majority of the differentially acetylated oxidative phosphorylation proteins were found to be in complexes 1 and 5 (Figure 4H). These complexes catalyze, respectively, the production of NAD^+ and ATP (Lenaz et al., 2006). This could suggest aberrant mitochondrial activity in shPab muscles. In agreement, previously we reported reduced mitochondrial membrane potential in shPab muscle cell culture (Anvar et al., 2013). Acetylation of mitochondrial proteins is achieved by the NAD^+-dependent deacetylases (sirtuins), among which SIRT1 is suggested to be central in aging-associated metabolic changes in muscles (Chang and Guarente, 2014).

PABPN1 Regulates SIRT1 mRNA Processing

We then examined SIRT1 levels in shPab muscles and found an elevated protein expression in shPab compared with scram muscles (Figures 5A and 5B). Interestingly, SIRT1 fold changes related to PABPN1 fold changes (Figure 5B). Therefore next we investigated whether SIRT1 is regulated by PABPN1 in an established PABPN1 knockdown muscle cell culture (de Klerk et al., 2012). SIRT1 protein levels were also elevated in shPab cell culture (Figure 5C). Thus we examined whether *Sirt1* transcript level is directly regulated by PABPN1. APA was determined with the ratio between two primer sets to distal and proximal region in *Sirt1* 3′ UTR (Figure 5D). We found a lower distal to proximal ratio in shPab cell culture (Figure 5E), indicating APA utilization. APA often resulted in shorter transcripts that are more stable (de Klerk et al., 2012; Jenal et al., 2012). Using the proximal primer set we found higher *Sirt1* mRNA levels in shPab cell culture (Figure 5F). Consistently, also in the OPMD mouse model (A17.1) we found APA and higher levels in *Sirt1* mRNA (Figure S6). Interestingly, APA and higher *Sirt1* expression were only found in fast-twitch quadriceps, but not in slow-twitch soleus (Figure S6). In this mouse model, soleus is also less affected (Trollet et al., 2010).

Next, we investigated whether *Sirt1* mRNA is directly regulated by APA utilization. We designed antisense oligonucleotides (AONs) specific to the proximal polyadenylation signal (PAS) in *Sirt1* 3′ UTR or scrambled AON (Figure 5G; Related to Table S7). The AONs were transfected into cell cultures, and masking of proximal PAS was assessed using the distal to proximal ratio. Compared with scrambled AON, the distal to proximal ratio was higher in *Sirt1*-AONs in shPab cell culture (Figure 5H), and consistently, *Sirt1* long transcript levels were also elevated (Figure 5I). Together this suggests that in conditions with reduced PABPN1 levels *Sirt1* levels are modulated via APA utilization. In control cells, *Sirt1* mRNA was also elevated after *Sirt1*-AON transfection, which was not due to APA utilization (Figures 5H and 5I), suggesting that additional factors affect the stability of long *Sirt1* transcript.

SIRT1 Inhibition Elevates PABPN1 Expression in shPab Cell Culture

Next, we investigated whether SIRT1 inhibition could reverse mitochondrial activity in shPab cell culture. Treatment with sirtinol, a SIRT1 inhibitor (Villalba and Alcaín, 2012), caused an increase in mitochondrial membrane potential in shPab cell culture (Figure 6A). Also, in shPab cell cultures that were treated with *Sirt1*-AON we found an increase in mitochondrial membrane potential (Figure S7). In addition, sirtinol treatment restored muscle cell fusion in shPab cell culture (Figure 6B). Consistently, increased cell fusion was also found in stable SIRT1 knockdown cell culture (Figure S8). This suggests that inhibition of SIRT1 activity restores PABPN1-mediated myogenic defects.

We then explored if SIRT1 inhibition affects PABPN1 function. We found that PABPN1 protein levels were elevated in a dose-dependent manner with 10 μM as the optimal sirtinol concentration (Figure S9). Consistently, PABPN1 increased in scram and shPab cells treated with sirtinol (Figure 6C). Consistently, PABPN1 levels were also increased in SIRT1 knockdown muscle cell culture (Figure S8). Sirtinol treatment also elevated the levels of nuclear PABPN1 in shPab cell culture (Figure 6D). As nuclear PAPBN1 regulates APA utilization, we determined the distal to proximal ratio of *Sirt1* mRNA in sirtinol-treated cells, and found a reversion compared with shPab cell culture (Figure 6E). Consistently, *Sirt1* fold change was also reduced (Figure 6F). In a recent study we showed that PABPN1 also regulates levels of several autophagy-related genes (Raz et al., 2017). Sirtinol treatment also restored levels of four of five autophagy-related genes (Figure 6F). Together, the results suggest that sirtinol treatment restores PABPN1 levels and its activity. Hence, this treatment could be beneficial in conditions with reduced PABPN1 levels.

Sirtinol Treatment Restores PABPN1-Mediated Muscle Wasting

We then investigated the effect of sirtinol treatment in shPab muscles. Sirtinol or empty vehicle was contralaterally injected into shPab muscles of three mice (Figure 7A). Treatment was repeated twice, and

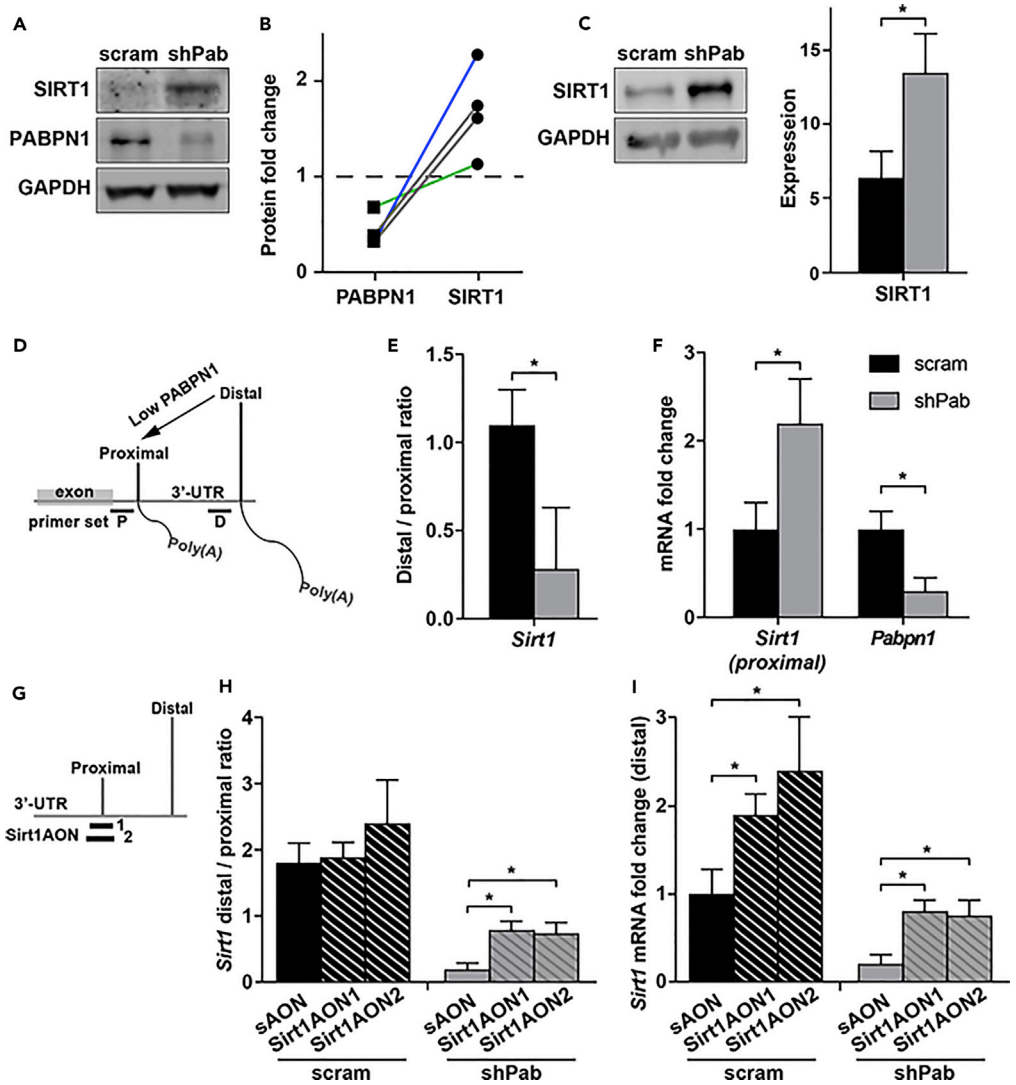

Figure 5. *Sirt1* mRNA Levels Are PABPN1-Regulated via Alternative PAS in the 3′ UTR

(A and B) SIRT1 levels in muscles of four mice. (A) A representative western blot in scram and shPab muscles. GAPDH is used as a loading control and for normalization. (B) Paired analysis of PABPN1 and SIRT1 fold change. Line connects values with a mouse. Mice with the smallest and highest PABPN1 fold changes are depicted with green and blue lines, respectively.

(C) A representative western blot in muscle cell culture. GAPDH was used as loading control. GAPDH-normalized values are plotted in the bar chart.

(D) A schematic presentation of alternative PAS utilization in the 3′ UTR in conditions with reduced PABPN1 levels. The positions of distal (D) and proximal (P) primer sets in *Sirt1* mRNA are depicted.

(E and F) Distal to proximal ratio in *Sirt1* 3′ UTR (E) and *Sirt1* fold change (F) in scram or shPab muscle cell cultures. Fold change was calculated after normalization to *Hprt* housekeeping gene and scram control. Statistical difference was assessed with the Student's t test. $p < 0.05$.

(G) A schematic presentation showing the position of *Sirt1* AONs. AONs are designed to mask proximal PAS in *Sirt1* mRNA.

(H and I) Bar charts show the distal to proximal ratio in *Sirt1* 3′ UTR (H) and the *Sirt1* fold change (I). Scrambled AON is depicted in the black bar, and with Sirt1 AONs are depicted in dashed bars. Fold change (I) was calculated after normalization to *Hprt* housekeeping gene and scram control. Averages and standard deviations of all the experiments here are from three biological replicates. Statistical difference was assessed with the Student's t test. $p < 0.05$.

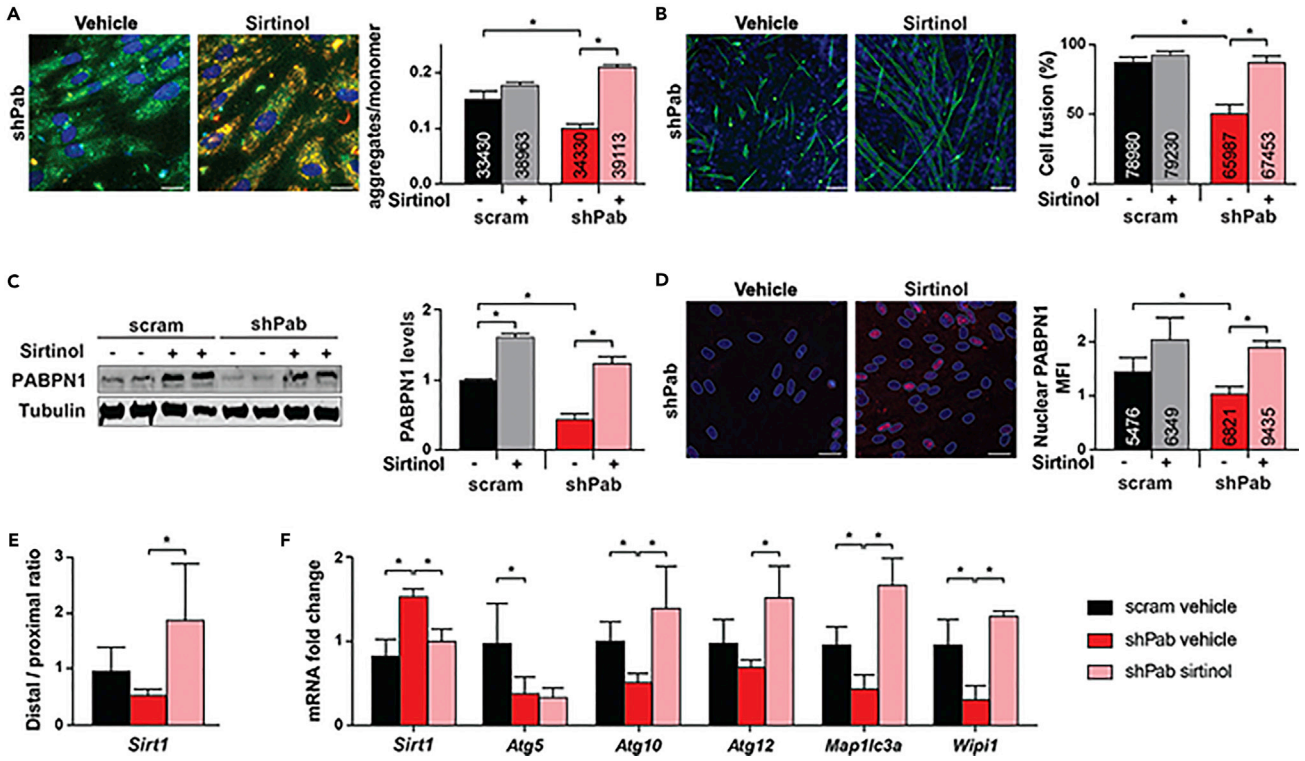

Figure 6. Sirtinol Treatment Reverses Myogenic Defects in shPab Muscle Cell Culture

(A) Mitochondrial membrane potential in shPab vehicle and sirtinol-treated muscle cell cultures. Images show an overlay between monomers (green) and J-aggregates (red) and the nuclei (blue). Scale bar, 10 μm. The ratio is measured from >30,000 cells.

(B) Muscle cell fusion in shPab vehicle and sirtinol-treated cell cultures. Images show an overlay between MyHC staining (green) and the nuclei (blue). Scale bar, 20 μm. The fraction of nuclei within MyHC regions is from >50,000 nuclei.

(C) Western blot analysis of PABPN1 levels in sirtinol-treated scram and shPab cell cultures. Tubulin is used as loading control and for normalization.

(D) Accumulation of nuclear PABPN1. Images show an overlay between PABPN1 (red) and nuclei (blue) in shPab vehicle and sirtinol-treated cell cultures. The segmented nuclei are depicted with a blue line. Scale bar, 10 μm. Bar chart shows the average MFI of nuclear PABPN1 from >50,000 nuclei.

(E and F) Distal to proximal ratio in *Sirt1* 3′ UTR (E) or mRNA fold change (F) in mock and sirtinol-treated shPab cell cultures. Fold change was calculated after normalization to *Hprt* and scram mock. Averages and standard deviations are from three biological replicates (A, B, D, E, F, and C, respectively). Statistical difference was assessed with the Student's t test. *p < 0.05.

muscles were harvested for *ex vivo* analyses (Figure 7A). Same as in cell culture, PABPN1 protein levels were increased in sirtinol-treated muscles (Figures 7B and 7C). In the sirtinol-treated shPab muscles ECM thickening was reduced and split myofibers were absent (Figure 7D). In addition, we observed a strong trend wherein the percentage of central nuclei decreased in sirtinol-treated muscles and myofiber cross-sectional area increased (Figures 7E and 7F). Previously we reported a shift in myofiber typing in shPab muscles: myosin-heavy chain (MyHC)-2b reduced, but MyHC-2a slightly increased (Riaz et al., 2016). Sirtinol treatment restored myofiber typing: MyHC-2b was elevated and MyHC-2a was reduced (Figure 7G). Last, we also noticed that MyHC-2b foci were formed in shPab muscles, which were completely absent in scram muscles (Figure S10). This was consistent with our previous study (Riaz et al., 2016). MyHC-2b foci are formed by the loss of *ACTN3* (MacArthur et al., 2007). In agreement, reduced ACTN3 protein levels were found in the shPab proteome (related to Table S3). The number and size of MyHC-2b foci were decreased in sirtinol-treated shPab muscles (Figure 7H). Taken together, this suggests that sirtinol treatment could be beneficial in PABPN1-mediated muscle wasting.

DISCUSSION

Muscle wasting is characterized by multiple histological alterations such as, atrophy, regeneration, thickening of the ECM, and switches in myofiber typing. Dysregulation of pathways regulating protein homeostasis, like the UPS and autophagy, play a role in muscle atrophy (Schiaffino et al., 2013). Reduced PABPN1 levels regulate expression levels of UPS, autophagy, and mitochondrial genes via APA utilization in the 3′

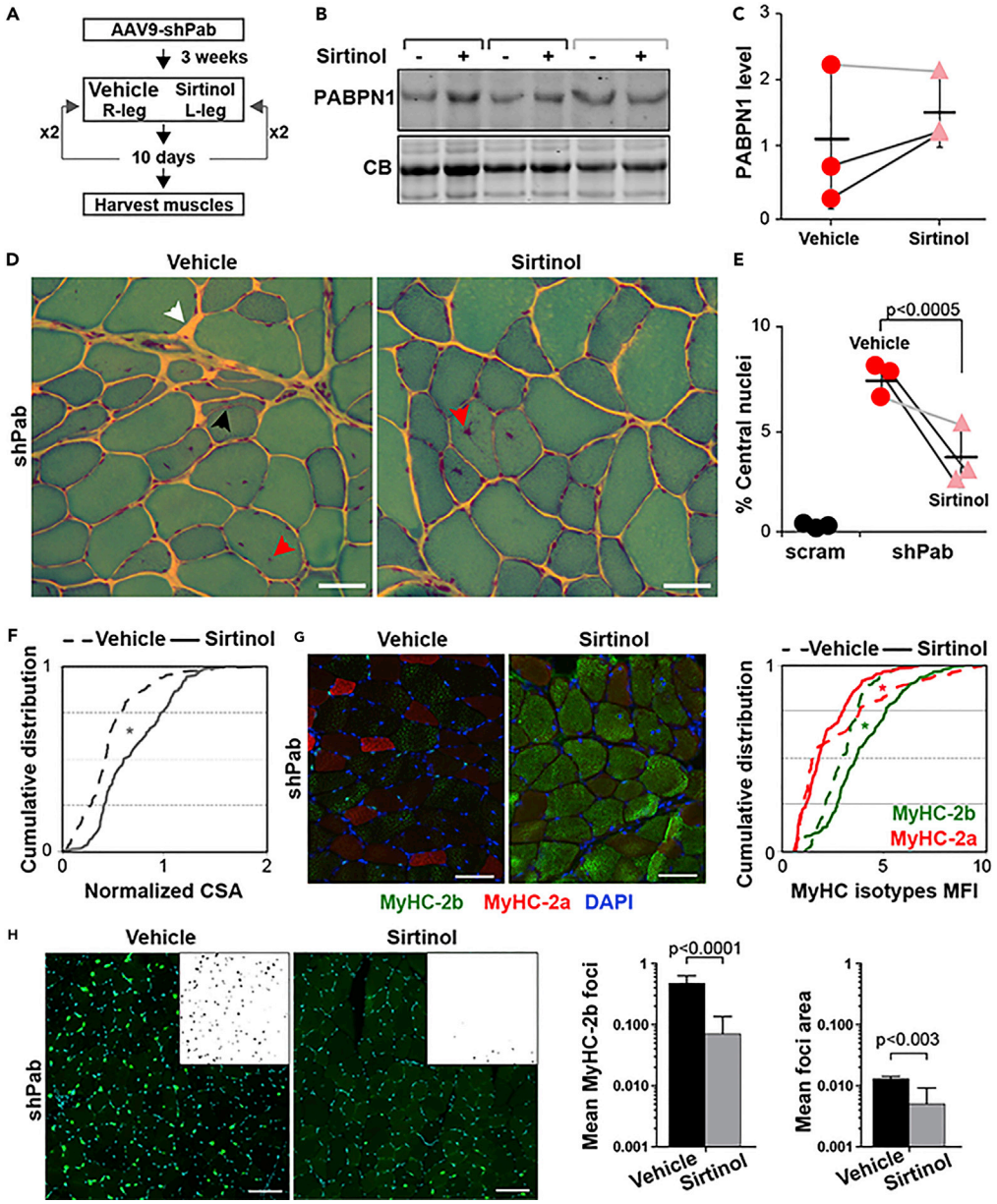

Figure 7. Sirtinol Treatment in shPab Muscles Reverses PABPN1-Induced Muscle Pathology

(A) An overview of sirtinol treatment in shPab muscles. Muscles were injected with AAV9 shPab in both right and left tibialis anterior muscles in three mice. After 3 weeks muscles were injected twice, with a 10-day interval, with empty vehicle or sirtinol.

(B) A representative western blot shows PABPN1 protein levels in shPab vehicle and sirtinol-injected muscles. Equal loading is assessed with Coomassie blue (CB). The mouse with the lowest PABPN1 fold change is depicted with a light gray line.

(C) Dot plot shows normalized PABPN1 expression levels. Lines connect paired muscles. Means and standard deviations are depicted with a black line.

(D) Gomori trichrome staining in muscle cryosections. Extracellular thickening is depicted with a white arrow, examples of central myonuclei and split myofibers are indicated with red and black arrows, respectively. Scale bar, 20 μm.

(E) Dot plot shows the fraction of central nuclei in mock and sirtinol-treated shPab muscles; >1,500 myofibers were counted per condition per mouse. Lines connect between paired muscles. Control AAV9 scrambled shRNA was injected into tibialis anterior TA (N = 4 muscles). Means and standard deviations are depicted with a black line.

(F) Cumulative distribution plot of myofiber cross-sectional area (CSA) in vehicle and sirtinol-treated muscles.

(G) Myofiber typing: Images show an overlay of MyHC-2b (green), MyHC-2a (red), and DAPI (blue) staining in vehicle or sirtinol-treated shPab muscles. Scale bar, 20 μm. Cumulative distribution plot of MyHC-2a and MyHC-2b MFI in single

Figure 7. *Continued*

myofibers from mock or sirtinol-treated muscles. Statistical difference was determined with the Kolmogorov-Smirnov test; *p < 0.0005.

(H) Representative images of MyHC-2b foci in vehicle and sirtinol-treated shPab muscles. Scale bar, 50 μm. The upper right box shows segmented MyHC-2b foci. Chart bars show mean MyHC-2b foci per myofiber (left panel) and mean foci area (right panel). Statistical difference was assessed with the Student's t test. (F–H) Pooled myofibers from all muscles, number of single myofibers > 1,000.

UTR, which consequently lead to reduced activity of all the cellular machineries (Chartier et al., 2015; Raz et al., 2017; Riaz et al., 2016). Reduced PABPN1 levels cause myogenic defects in muscle cell culture (Anvar et al., 2013; Apponi et al., 2010). Moreover, muscle wasting is found in mouse models for OPMD (Trollet et al., 2010; Vest et al., 2017). ECM thickening and central nuclei were also reported in affected OPMD muscles (Raz et al., 2013). Also, in shPab muscles we found ECM thickening and central nuclei, suggesting that reduced PABPN1 levels cause multiple pathological features of muscle wasting and myogenic defects.

PABPN1 regulates mRNA processing, yet it is not fully understood how an altered transcriptome leads to muscle wasting pathology. Recently we showed that transcripts from APA in the 3′ UTR are under-represented in the translation machinery (Raz et al., 2017). Substantial discrepancies between mRNA fold changes and translation efficiency were also reported in muscle cell cultures (de Klerk et al., 2015). Here we found only limited correlation between transcript and protein fold changes in the same muscles. In agreement, limited overlap between transcriptome and proteome was also reported in muscles from aged adults (Robinson et al., 2017). Limited correlation between outcomes from RNA-seq-based transcriptome and mass-spectrometry-based proteome could be affected by technical issues and in-depth differences. Noteworthy is that for the more affected genes (fold change |>1.5|), variation of their corresponding proteins is generally of a greater magnitude. This suggests that despite a genome-wide effect of PABPN1 on mRNA processing, only a subset of transcripts affect the muscle pathology. Higher protein fold changes in shPab muscles are consistent with lower proteasome activity and reduced autophagosome formation (Raz et al., 2017; Riaz et al., 2016). Posttranscriptional drivers of muscle wasting are associated with protein breakdown regulated by the ubiquitin proteasome and autophagy lysosome pathways (Schiaffino et al., 2013). Also, in aging muscles and in OPMD models, dysregulation of protein homeostasis seems to play a central role (Anvar et al., 2011b; Murgia et al., 2017; Raz et al., 2013; Vest et al., 2017). A broader effect on protein catabolism is implicated by higher levels of the ribosomal proteins in aging muscles, shPab muscles, and OPMD models (Murgia et al., 2017; Robinson et al., 2017; Vest et al., 2017). In addition, reduced expression of mitochondrial proteins is also commonly found in shPab, OPMD, and aged muscles (Murgia et al., 2017; Robinson et al., 2017; Vest et al., 2017). In OPMD muscles, reduced mitochondrial activity is correlated with APA utilization in a subset of mitochondrial genes (Chartier et al., 2015). Mitochondrial activity is more robustly regulated by reversible acetylation (Baeza et al., 2016). Acetylation of mitochondrial proteins is common in skeletal muscles (Lundby et al., 2012). Differential acetylation of mitochondrial proteins was found to be prominent in atrophic rat muscles (Ryder et al., 2015), and consistently also in shPab muscles, with complexes I and V being the most affected. NAD^+ production is carried out in complex I, and sirtuins activity is NAD^+ dependent. We show that deacetylation inhibition by sirtinol treatment in shPab restored mitochondrial membrane potential and myogenic defects.

Acetylation affects protein levels and function, among which the effect on metabolic processes is widely studied (Drazic et al., 2016). Acetylation is regulated by the sirtuins NAD^+-dependent deacetylase gene family (Imai and Guarente, 2016). SIRT1 facilitates metabolic benefits in various cells across different tissues, and a central role in aging muscles was elucidated in many studies (Chang and Guarente, 2014). The mechanisms regulating SIRT1 levels in aging tissues are inadequately understood. Here we show that SIRT1 levels are directly tuned by PABPN1 via APA in the 3′ UTR. Masking the proximal polyadenylation site using specific AONs restored APA in SIRT1 and mitochondrial membrane potential in shPab muscle cell culture. Masking APA using oligonucleotides to pathogenic molecules was suggested as a specific silencing approach (Chen et al., 2016; Marsollier et al., 2016; Raz et al., 2014). Moreover, SIRT1 inhibition restored PABPN1 levels, PABPN1 function, and myogenesis defects, suggesting that SIRT1, directly or indirectly, regulates PABPN1 levels. Acetylated PABPN1 was identified in the SIRT1-dependent acetylome (Scholz et al., 2015), suggesting that PABPN1 could be modulated by SIRT1-dependent deacetylation. Yet, how acetylation of PABPN1 affects its level and function should be explored in future studies. Nevertheless, we show that acetylation inhibition restored muscle wasting in shPab. Our results are consistent with studies suggesting that restoring NAD^+ levels or targeting SIRT1 could ameliorate the age-associated

disorders (Giblin et al., 2014; Villalba and Alcaín, 2012) (Tarragó et al., 2018). Moreover, sirtinol has been shown to reduce aggregation of the expanded PABPN1 in a *C. elegans* model for OPMD (Catoire et al., 2008; Pasco et al., 2010). In prokaryotes, increased acetylation leads to enhanced aggregation and formation of inclusion bodies (Kuczynska-Wisnik et al., 2016). Whether deacetylation directly affects protein aggregation in muscles needs to be investigated in future studies.

Taken together, we show that muscle wasting, atrophy, and regeneration are induced by reduced PABPN1 levels. The shPab proteome shows a modulated protein acetylation profile, and the shPab acetylome is predominantly hypoacetylated. Reduced protein acetylation is consistent with higher SIRT1 levels. We show that *Sirt1* mRNA is regulated by PABPN1, and in turn, SIRT1 inhibition or knockdown elevates PABPN1 protein levels and restores PABPN1 molecular function. Consequently, cellular defects and muscle wasting are repaired in conditions with reduced PABPN1 levels. Our study suggests that maintaining physiological levels of both PABPN1 and SIRT1 is beneficial for muscles, and disturbance causes muscle wasting. This is the first study showing that reduced PABPN1 levels broadly affect protein acetylation. Future studies in other models and possibly in human aging muscles will further validate the role of PABPN1 in the protein acetylation landscape and its effect on muscle wasting.

Limitations of the Study

This study presents the role of protein deacetylation in a mouse model, which was generated by AAV9-expressing shRNA to PABPN1. Our study design allowed paired analysis, excluding inter-mice variations. Yet, parts of this study should be replicated in other models. Recently, two other mouse models for PABPN1 were published (Vest et al., 2017), and these should be considered in future studies. The role of protein deacetylation in aging muscles should be further studied in human muscles.

METHODS

All methods can be found in the accompanying Transparent Methods supplemental file.

SUPPLEMENTAL INFORMATION

Supplemental Information includes Transparent Methods, 13 figures, and 10 tables and can be found with this article online at https://doi.org/10.1016/j.isci.2019.01.024.

A video abstract is available at https://doi.org/10.1016/j.isci.2019.01.024#mmc6.

ACKNOWLEDGMENTS

We thank Dr. Roman Fischer and Simon Davis from the Discovery Proteomics Facility within the TDI Mass Spectrometry Laboratory for their expert help and advice with the proteomics analysis. This study is supported by the AFM-Telethon # 21160 to V.R. and by the Prinses Beatrix Spierfonds to V.R. and C.S.O. The B.M.K. lab was supported by the Engineering and Physical Sciences Research Council, United Kingdom (EP/N034295/1). The funders had no role in study design, data collection and analysis, decision to publish, or preparation of the manuscript.

AUTHOR CONTRIBUTIONS

The mouse model was generated by M.R. RNA-seq analysis was carried out by S.M.K. and V.R. Mass spectrometry and proteome study were carried out by C.S.O., R.K., P.D.C., A.P.-F. and B.M.K. Cell culture studies were carried out by C.S.O. and V.R. AONs were designed by A.A.-R. V.R. designed the study and made funding available. The manuscript was written by C.S.O. and V.R, and all authors commented on the manuscript.

DECLARATION OF INTERESTS

All authors declare no conflict of interest.

Received: August 15, 2018
Revised: November 4, 2018
Accepted: January 15, 2019
Published: February 22, 2019

REFERENCES

Anvar, S.Y., Raz, Y., Verway, N., van der Sluijs, B., Venema, A., Goeman, J.J., Vissing, J., van der Maarel, S.M., t Hoen, P.A., van Engelen, B.G., et al. (2013). A decline in PABPN1 induces progressive muscle weakness in oculopharyngeal muscle dystrophy and in muscle aging. Aging (Albany NY) *5*, 412–426.

Anvar, S.Y., t Hoen, P.A., Venema, A., van der Sluijs, B., van Engelen, B., Snoeck, M., Vissing, J., Trollet, C., Dickson, G., Chartier, A., et al. (2011a). Deregulation of the ubiquitin-proteasome system is the predominant molecular pathology in OPMD animal models and patients. Skelet. Muscle *1*, 15.

Anvar, S.Y., Tucker, A., Vinciotti, V., Venema, A., van Ommen, G.-J.B., van der Maarel, S.M., Raz, V., and 't Hoen, P.A.C. (2011b). Interspecies translation of disease networks increases robustness and predictive accuracy. PLoS Comput. Biol. *7*, e1002258.

Apponi, L.H., Leung, S.W., Williams, K.R., Valentini, S.R., Corbett, A.H., and Pavlath, G.K. (2010). Loss of nuclear poly(A)-binding protein 1 causes defects in myogenesis and mRNA biogenesis. Hum. Mol. Genet. *19*, 1058–1065.

Baeza, J., Smallegan, M.J., and Denu, J.M. (2016). Mechanisms and dynamics of protein acetylation in mitochondria. Trends Biochem. Sci. *41*, 231–244.

Banerjee, A., Apponi, L.H., Pavlath, G.K., and Corbett, A.H. (2013). PABPN1: molecular function and muscle disease. FEBS J. *280*, 4230–4250.

Bowen, T.S., Schuler, G., and Adams, V. (2015). Skeletal muscle wasting in cachexia and sarcopenia: molecular pathophysiology and impact of exercise training. J. Cachexia Sarcopenia Muscle *6*, 197–207.

Brais, B., Bouchard, J.-P., Xie, Y.-G., Rochefort, D.L., Chretien, N., Tome, F.M.S., Lafrentere, R.G., Rommens, J.M., Uyama, E., Nohira, O., et al. (1998). Short GCG expansions in the PABP2 gene cause oculopharyngeal muscular dystrophy. Nat. Genet. *18*, 164–167.

Catoire, H., Pasco, M.Y., Abu-Baker, A., Holbert, S., Tourette, C., Brais, B., Rouleau, G.A., Parker, J.A., and Neri, C. (2008). Sirtuin inhibition protects from the polyalanine muscular dystrophy protein PABPN1. Hum. Mol. Genet. *17*, 2108–2117.

Chang, H.-C., and Guarente, L. (2014). SIRT1 and other sirtuins in metabolism. Trends. Endocrinol. Metab. *25*, 138–145.

Chartier, A., Klein, P., Pierson, S., Barbezier, N., Gidaro, T., Casas, F., Carberry, S., Dowling, P., Maynadier, L., Bellec, M., et al. (2015). Mitochondrial dysfunction reveals the role of mRNA poly(A) tail regulation in oculopharyngeal muscular dystrophy pathogenesis. PLoS Genet. *11*, e1005092.

Chen, J.C., King, O.D., Zhang, Y., Clayton, N.P., Spencer, C., Wentworth, B.M., Emerson, C.P., Jr., and Wagner, K.R. (2016). Morpholino-mediated knockdown of DUX4 toward facioscapulohumeral muscular dystrophy therapeutics. Mol. Ther. *24*, 1405–1411.

Cohen, S., Nathan, J.A., and Goldberg, A.L. (2014). Muscle wasting in disease: molecular mechanisms and promising therapies. Nat. Rev. Drug Discov. *14*, 58–74.

de Klerk, E., Fokkema, I.F., Thiadens, K.A., Goeman, J.J., Palmblad, M., den Dunnen, J.T., von Lindern, M., and t Hoen, P.A. (2015). Assessing the translational landscape of myogenic differentiation by ribosome profiling. Nucleic Acids Res. *43*, 4408–4428.

de Klerk, E., Venema, A., Anvar, S.Y., Goeman, J.J., Hu, O., Trollet, C., Dickson, G., den Dunnen, J.T., van der Maarel, S.M., Raz, V., et al. (2012). Poly(A) binding protein nuclear 1 levels affect alternative polyadenylation. Nucleic Acids Res. *40*, 9089–9101.

Drazic, A., Myklebust, L.M., Ree, R., and Arnesen, T. (2016). The world of protein acetylation. Biochim. Biophys. Acta *1864*, 1372–1401.

Giblin, W., Skinner, M.E., and Lombard, D.B. (2014). Sirtuins: guardians of mammalian healthspan. Trends Genet. *30*, 271–286.

Imai, S.-i., and Guarente, L. (2016). It takes two to tango: NAD(+) and sirtuins in aging/longevity control. NPJ Aging Mech. Dis. *2*, 16017.

Jenal, M., Elkon, R., Loayza-Puch, F., van Haaften, G., Kuhn, U., Menzies, F.M., Oude Vrielink, J.A., Bos, A.J., Drost, J., Rooijers, K., et al. (2012). The poly(A)-binding protein nuclear 1 suppresses alternative cleavage and polyadenylation sites. Cell *149*, 538–553.

Kawano, F., Nimura, K., Ishino, S., Nakai, N., Nakata, K., and Ohira, Y. (2015). Differences in histone modifications between slow- and fast-twitch muscle of adult rats and following overload, denervation, or valproic acid administration. J. Appl. Physiol. (1985) *119*, 1042–1052.

Kuczynska-Wisnik, D., Moruno-Algara, M., Stojowska-Swedrzynska, K., and Laskowska, E. (2016). The effect of protein acetylation on the formation and processing of inclusion bodies and endogenous protein aggregates in Escherichia coli cells. Microb. Cell Fact. *15*, 189.

Lenaz, G., Fato, R., Genova, M.L., Bergamini, C., Bianchi, C., and Biondi, A. (2006). Mitochondrial complex I: structural and functional aspects. Biochim. Biophys. Acta *1757*, 1406–1420.

Lepper, C., Partridge, T.A., and Fan, C.M. (2011). An absolute requirement for Pax7-positive satellite cells in acute injury-induced skeletal muscle regeneration. Development *138*, 3639–3646.

Lundby, A., Lage, K., Weinert, Brian T., Bekker-Jensen, Dorte B., Secher, A., Skovgaard, T., Kelstrup, Christian D., Dmytriyev, A., Choudhary, C., Lundby, C., et al. (2012). Proteomic analysis of lysine acetylation sites in rat tissues reveals organ specificity and subcellular patterns. Cell Rep. *2*, 419–431.

MacArthur, D.G., Seto, J.T., Raftery, J.M., Quinlan, K.G., Huttley, G.A., Hook, J.W., Lemckert, F.A., Kee, A.J., Edwards, M.R., Berman, Y., et al. (2007). Loss of ACTN3 gene function alters mouse muscle metabolism and shows evidence of positive selection in humans. Nat. Genet. *39*, 1261–1265.

Marsollier, A.C., Ciszewski, L., Mariot, V., Popplewell, L., Voit, T., Dickson, G., and Dumonceaux, J. (2016). Antisense targeting of 3' end elements involved in DUX4 mRNA processing is an efficient therapeutic strategy for facioscapulohumeral dystrophy: a new gene-silencing approach. Hum. Mol. Genet. *25*, 1468–1478.

Murgia, M., Toniolo, L., Nagaraj, N., Ciciliot, S., Vindigni, V., Schiaffino, S., Reggiani, C., and Mann, M. (2017). Single muscle fiber proteomics reveals fiber-type-specific features of human muscle aging. Cell Rep. *19*, 2396–2409.

Pasco, M.Y., Rotili, D., Altucci, L., Farina, F., Rouleau, G.A., Mai, A., and Neri, C. (2010). Characterization of sirtuin inhibitors in nematodes expressing a muscular dystrophy protein reveals muscle cell and behavioral protection by specific sirtinol analogues. J. Med. Chem. *53*, 1407–1411.

Raz, V., Buijze, H., Raz, Y., Verwey, N., Anvar, S.Y., Aartsma-Rus, A., and van der Maarel, S.M. (2014). A novel feed-forward loop between ARIH2 E3-ligase and PABPN1 regulates aging-associated muscle degeneration. Am. J. Pathol. *184*, 1119–1131.

Raz, V., Dickson, G., and t Hoen, P.A.C. (2017). Dysfunctional transcripts are formed by alternative polyadenylation in OPMD. Oncotarget *8*, 73516–73528.

Raz, V., Routledge, S., Venema, A., Buijze, H., van der Wal, E., Anvar, S., Straasheijm, K.R., Klooster, R., Antoniou, M., and van der Maarel, S.M. (2011). Modeling oculopharyngeal muscular dystrophy in myotube cultures reveals reduced accumulation of soluble mutant PABPN1 protein. Am. J. Pathol. *179*, 1988–2000.

Raz, V., Sterrenburg, E., Routledge, S., Venema, A., van der Sluijs, B.M., Trollet, C., Dickson, G., van Engelen, B.G., van der Maarel, S.M., and Antoniou, M.N. (2013). Nuclear entrapment and extracellular depletion of PCOLCE is associated with muscle degeneration in oculopharyngeal muscular dystrophy. BMC Neurol. *13*, 1–13.

Riaz, M., Raz, Y., van Putten, M., Paniagua-Soriano, G., Krom, Y.D., Florea, B.I., and Raz, V. (2016). PABPN1-dependent mRNA processing induces muscle wasting. PLoS Genet. *12*, e1006031.

Robinson, M.M., Dasari, S., Konopka, A.R., Johnson, M.L., Manjunatha, S., Esponda, R.R., Carter, R.E., Lanza, I.R., and Nair, K.S. (2017). Enhanced protein translation underlies improved metabolic and physical adaptations to different exercise training modes in young and old humans. Cell Metab. *25*, 581–592.

Ryder, D.J., Judge, S.M., Beharry, A.W., Farnsworth, C.L., Silva, J.C., and Judge, A.R. (2015). Identification of the acetylation and ubiquitin-modified proteome during the progression of skeletal muscle atrophy. PLoS One *10*, e0136247.

Sambasivan, R., Yao, R., Kissenpfennig, A., Van Wittenberghe, L., Paldi, A., Gayraud-Morel, B.,

Guenou, H., Malissen, B., Tajbakhsh, S., and Galy, A. (2011). Pax7-expressing satellite cells are indispensable for adult skeletal muscle regeneration. Development *138*, 3647–3656.

Schiaffino, S., Dyar, K.A., Ciciliot, S., Blaauw, B., and Sandri, M. (2013). Mechanisms regulating skeletal muscle growth and atrophy. FEBS J. *280*, 4294–4314.

Schiaffino, S., Rossi, A.C., Smerdu, V., Leinwand, L.A., and Reggiani, C. (2015). Developmental myosins: expression patterns and functional significance. Skelet. Muscle *5*, 22.

Scholz, C., Weinert, B.T., Wagner, S.A., Beli, P., Miyake, Y., Qi, J., Jensen, L.J., Streicher, W., McCarthy, A.R., Westwood, N.J., et al. (2015). Acetylation site specificities of lysine deacetylase inhibitors in human cells. Nat. Biotechnol. *33*, 415–423.

Tarragó, M.G., Chini, C.C.S., Kanamori, K.S., Warner, G.M., Caride, A., de Oliveira, G.C., Rud, M., Samani, A., Hein, K.Z., Huang, R., et al. (2018). A potent and specific CD38 inhibitor ameliorates age-related metabolic dysfunction by reversing tissue NAD+ decline. Cell Metab. *27*, 1081–1095.e10.

Trollet, C., Anvar, S.Y., Venema, A., Hargreaves, I.P., Foster, K., Vignaud, A., Ferry, A., Negroni, E., Hourde, C., Baraibar, M.A., et al. (2010). Molecular and phenotypic characterization of a mouse model of oculopharyngeal muscular dystrophy reveals severe muscular atrophy restricted to fast glycolytic fibres. Hum. Mol. Genet. *19*, 2191–2207.

Vest, K.E., Phillips, B.L., Banerjee, A., Apponi, L.H., Dammer, E.B., Xu, W., Zheng, D., Yu, J., Tian, B., Pavlath, G.K., et al. (2017). Novel mouse models of oculopharyngeal muscular dystrophy (OPMD) reveal early onset mitochondrial defects and suggest loss of PABPN1 may contribute to pathology. Hum. Mol. Genet. *26*, 3235–3252.

Villalba, J.M., and Alcaín, F.J. (2012). Sirtuin activators and inhibitors. Biofactors *38*, 349–359.

ISCI, Volume *12*

Supplemental Information

Deacetylation Inhibition Reverses PABPN1-Dependent Muscle Wasting

Cyriel S. Olie, Muhammad Riaz, Rebecca Konietzny, Philip D. Charles, Adan Pinto-Fernandez, Szymon M. Kiełbasa, A. Aartsma-Rus, Jelle J. Goeman, Benedikt M. Kessler, and Vered Raz

Supplemental Information (SI)

Supplemental Tables

Table S1. The shPab Transcriptome. Related to Fig. 2A

Table S2. Gene enrichment in shPab transcriptome. Related to Fig. 2A

A top list of the six most significant enriched gene ontology of the candidate with altered mRNA expression levels in shPab muscles (p<0.05, FDR).

Group term	Count	%	FDR	Genes
extracellular matrix	19	5.76	9.38E-07	
muscle organ development	13	3.94	2.33E-05	
mitochondrion	34	10.30	2.37E-03	
ribosome	10	3.03	2.47E-03	
actin binding	12	3.64	3.97E-03	
cytoskeleton	27	8.18	1.74E-02	

Table S3. The shPab Proteome. Related to Fig. 2B-C

Table S4. Protein enrichment in shPab proteome. Related to Fig. 3B

The table shows a top list of the six most significant enriched gene ontology of the candidate with altered protein expression levels in shPab muscles (p<0.05, FDR).

Group term	Count	%	FDR
Acetylation	**154**	**62.86**	**1.27E-67**
Phosphoprotein	174	71.02	6.46E-30
Mitochondrion	**59**	**24.08**	**2.95E-22**
Ribosomal protein	**18**	**7.35**	**1.04E-07**
Isopeptide bond	35	14.29	1.11E-06
Oxidoreductase	27	11.02	9.07E-06
Ubl conjugation	42	17.14	4.49E-05
Cytoskeleton	**34**	**13.88**	**7.37E-05**
Methylation	30	12.24	7.28E-04
Nucleotide-binding	**43**	**17.55**	**9.98E-04**
Glycolysis	**7**	**2.86**	**2.36E-03**
Muscle protein	**7**	**2.86**	**2.54E-02**

Highlighted in bold are the terms that are shown in the pie-chart (Figure 3B).

Table S5. The shPab Acetylome. Related to Fig. 4B

Table S6. A comparison of acetylome studies in skeletal muscles. Related to Fig. 4B

Table S7. shRNAs and AONs used for muscle injection or in myoblasts. Related to Methods.

Name	Gene	shRNA clone	Sequence
scram	*- (Scrambled)*	-	CCTGTACCGAGAAGTAGAAA
shPab	*Pabpn1*	TRCN0000102536	CCCTGTTCAGAGGAAGACAAA
shSIRT1	*Sirt1*	TRCN0000306512	

AON	Sequence (reverse compatible) (PAS is in red)	TM	ΔG (kcal/mol)	Binding energy:
Sirt1 AON1	GCCAUUGUUUAAUUAAA UACC	41.5	-17.4	24.5
Sirt1 AON2	GCCAUUGUUUAAUUAAA UACCUAUCAC	52.1	-10.2	33

Table S8: sequencing data quality raw data.

Sample	C-1	C-2	C-3	C-4	D-1	D-2	D-3	D-4	pvalue C vs. D
Total fastq records	30347688	30266763	36175552	23579726	38849366	31247162	35550883	30832354	0.17
insert size median	154	150	187	123	136	160	103	179	0.78
reads aligned and mapped	12087443	11620309	14648990	9487896	11366660	12654043	9387418	13118941	0.87

C=scram D=shPab, numbers indicates mouse number

Table S9. Primer and antibody list Related to Methods.

A. primers

Gene	Ensemble ID	Forward 5'-3'	Reverse 5'-3'
Hprt1	ENSMUSG00000025630	CGTCGTGATTAGCGATGATG	TTTTCCAAATCCTCGGCATA
Pabpn1	ENSMUSG00000022198	GCCTCACTTTTGAGGTGCTC	AGGGGAATACCATGATGTCG
Sirt1 distal	ENSMUSG00000020063	CCTGTTGAGGATTTGGTGT	GAACATTGCCCCCAAATTTA
Sirt1 proximal		TAAGCGGCTTGAGGGTAATC	CACATGCCAGAGTCCAAGTTT
Atg5	ENSMUSG00000038160	AGATGGACAGCTGCACACAC	GCTGGGGGACAATGCTAATA
Atg10	ENSMUSG00000021619	AAGCAACATCACAATCGGAGT	CTATTCCAAACAGGCTTCTGC
Atg12	ENSMUSG00000032905	CCCAGACCAAGAAGTTGGAA	CAGCACCGAAATGTCTCTGA
Map1lc3b (Lc3)	ENSMUSG00000031812	CATGAGCGAGTTGGTCAAGA	TTGACTCAGAAGCCGAAGGT
Wipi1	ENSMUSG00000041895	GCTCCGAGGGGAAGTTATTC	CCTCGTTCTCTCCAAAACCA
eMyh3	ENSMUSG00000020908	GGAAGACGGTGAACACCAAG	CCCTTCATTTTGGAGTCCTTC

B. antibodies for WB

Primary antibody	supplier	dilution factor
rabbit anti-PABPN1	LS-B8482, LS Bio, WA. USA	1:2000

mouse anti_SIRT1	ab110304, Abcam, CAM, UK	1:1000
rabbit anti-acetylated lysine	PA5-16190, ThermoFisher	1:1000
mouse anti-UCH-L1	sc-58594, Santa Cruz	1:1000
rabbit anti-USP14	sc-100630, Santa Cruz	1:1000
rabbit anti-UCH-L3	ab126703, Abcam, CAM, UK	1:1000
mouse anti-proteasome β-subunit 2 (PSB2	sc-58410, Santa Cruz, CA, USA	1:1000
rabbit anti-proteasome β-subunit 5 (PSB5)	#09–278, Millipore, MA, USA	1:1000
rabbit anti-OTUB1	10573-1-ap, Proteintech, MAN, UK	1:800
mouse anti-Ubiquitin	BML-PW0930-0100, Enzolife, EXE, UK	1:1000
rabbit anti-SUMO-2/3	4974, Cell Signaling, MA, USA	1:1000
mouse anti-GAPDH	MA5-15738 / Pierce	1:5000
mouse anti-actin	sc-8432; Santa Cruz	1:2000
rabbit anti-UBE2N	ab25885, Abcam, CAM, UK	1:1000
mouse anti-Tubulin	T6199; Sigma-Aldrich	1:2000
Secondary: IRDye 800CW or IRDye 680RD conjugated	LICOR, NE. USA	1:5000

Antibodies for IF

MyHC-2a, 594-conjugated	In house, (M.Riaz et al., 2015)	1:700
MyHC-2b, 488-conjugated		1:600
rabbit anti-acetylated lysine	PA5-16190, ThermoFisher	1:1000
MF20	Sigma Aldrich	1:250
mouse anti-Pax-7	DSHB	1:200
Secondary: rabbit anti Cy5-conjugated	ThermoFisher	1:5000

Table S10. Pearson correlation of Mass-spec technical replicates. Related to methods.

	Mouse 1		Mouse 2		Mouse 3		Mouse 4	
	scram	shPab	scram	shPab	scram	shPab	scram	shPab
R	0.9976	0.9994	0.9988	0.9986	0.9995	0.9979	0.9997	0.9994
95%	0.9973	0.9993	0.9986	0.9985	0.9994	0.9977	0.9996	0.9993
confidence	0.9979	0.9994	0.9989	0.9988	0.9995	0.9982	0.9997	0.9995

Supplemental Figures

Fig S1. Transduction efficiency of paired sample analysis investigating the effect of PABPN1 down-regulation. Related to Fig. 1A.

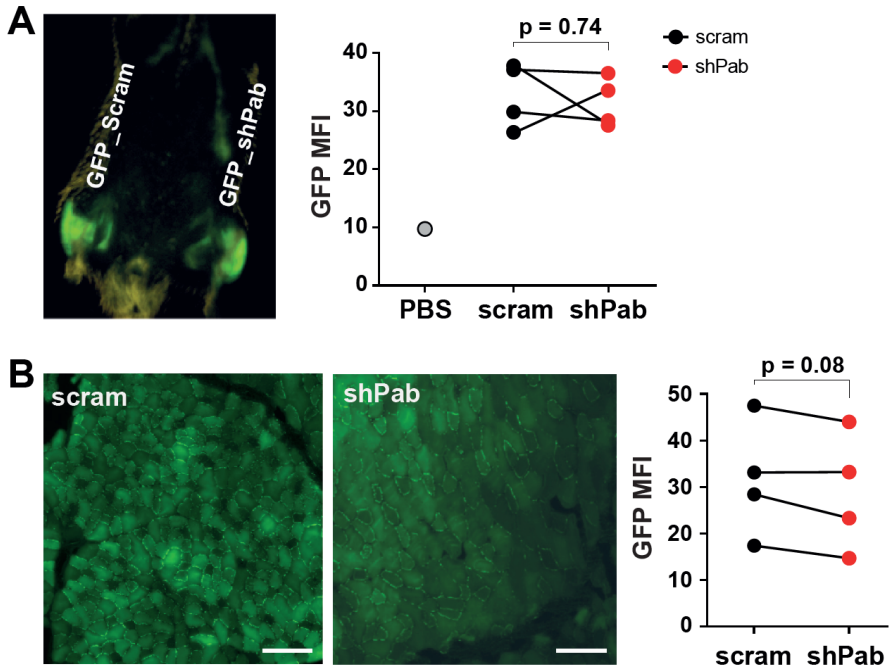

A. Contralateral AAV9 injection. Image shows GFP fluorescence in a representative mouse, five weeks after injection of AAV9 particles. GFP signal is confounded to TA muscles. Dot plot shows quantification of GFP MFI in AAV-injected TA muscles. Lines connect paired muscles per mouse. PBS injected muscles are control. **B.** GFP fluorescence in muscle cryosections. Images show representative area. Scale bar is 40 µm. Paired dot-plot shows average MFI GFP signal in cross-sections (5 images per muscle, N= 4 mice). P-values are calculated with the paired t-test.

Figure S2. Western blot analysis. Related to Fig. 2B.

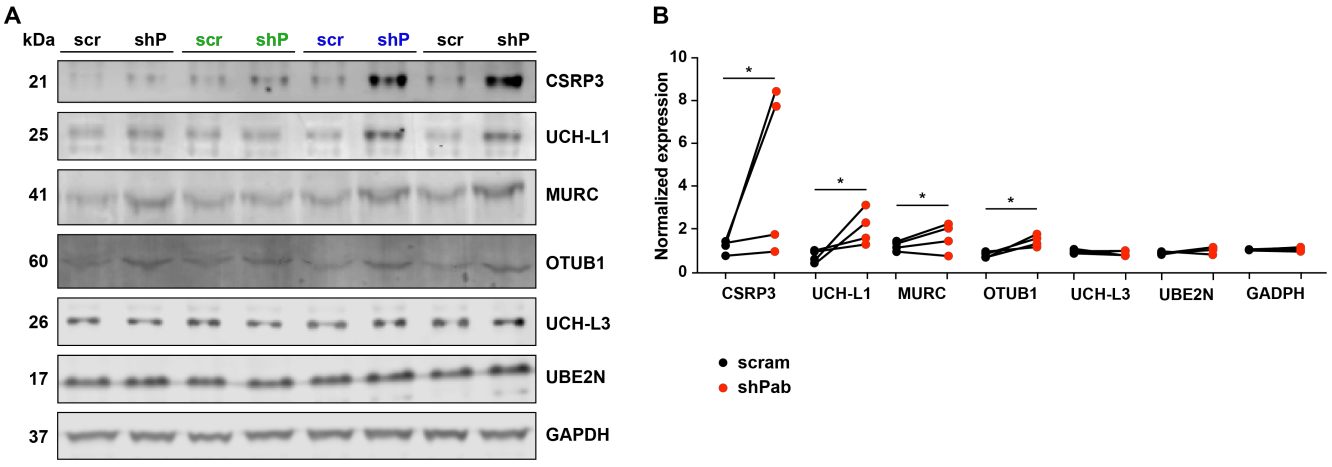

A. Western blot validation for seven proteins from the mass spectrometer. CSRP3, UCH-L1, MURC and OTUB1 were confirmed to be changing in the shPab proteome. WB of UCH-L3, UBE2N and GAPDH confirmed no change in their expression as detected by the mass spectrometer. Paired muscles are indicated. The mouse with the highest PABPN1 FC is depicted in blue and the lowest PABPN1 FC in green. **B.** Protein expression levels were normalized to GAPDH and the average of all

scram muscles. Paired analysis was carried out in N=4 mice. Statistical difference was determined with the paired t-test. $p<0.05$ in marked (*).

Figure S3. Density plots of average fold change in shPab transcriptome and proteome. Related to Fig. 3C-D.

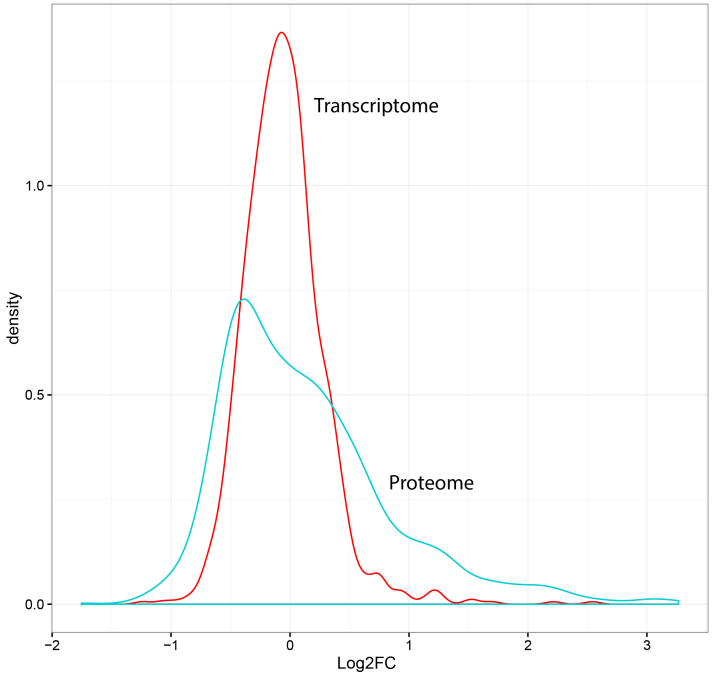

Density plot shows log2 fold change (FC) between scram and shPab muscles (N=4 mice) for the overlapping genes and proteins.

Figure S4. Hierarchal clustering of protein abundance. Related to Fig. 3.

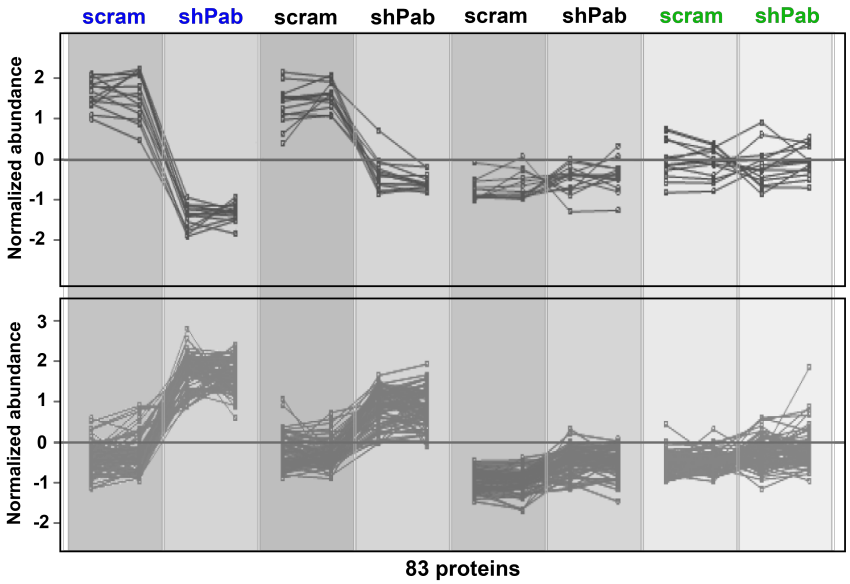

Normalized protein abundances plotted for 83 proteins that clustered according to PABPN1 fold change across N=4 mice. Values in technical replicates (N=2) in scram and shPab are shown for every muscle. Paired muscles are connected. The mouse with highest or lowest PABPN1 fold change is depicted in blue or green, respectively. Amongst the 83 proteins, ribosomal proteins were highly present (~25%) as well as cytoskeletal proteins (~18%). Two proteins, CSRP3 and UCH-L1 were validated using western blot (Fig. S2).

Figure S5. Protein acetylation in fast versus slow-twitch muscles. Related to Fig. 4C.

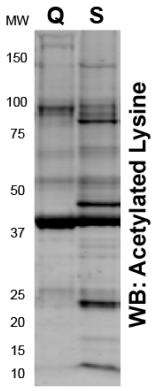

The western blot shows the bulk acetylation pattern between fast-twitch muscle: Quadriceps (Q) and slow-twitch muscle: Soleus (S) muscle protein extract.

Figure S6. *Sirt1* expression in A17.1 muscles. Related to Fig. 5A.

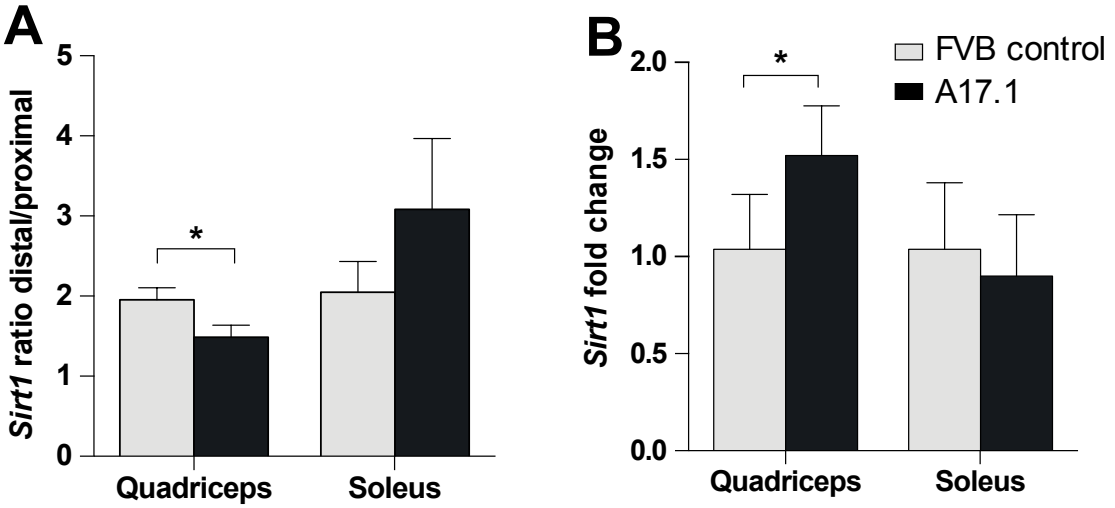

Sirt1 PAS utilization and mRNA levels in FVB control or A17.1 mouse, 6 weeks-old, was determined from quadriceps and soleus. **A.** Bar chart shows the ratio between PCR products from the distal and proximal primer sets. **B.** Bar chart shows *Sirt1* mRNA fold change in the same muscles. Fold change was calculated after normalization to *Hprt* housekeeping gene and FVB control. Averages and standard variations are from N=5. Statistical difference was assessed with the Student's t-test, $p<0.05$ is depicted with an asterisk.

Figure S7. *Sirt1*-AON restores mitochondrial membrane potential. Related to Fig. 6.

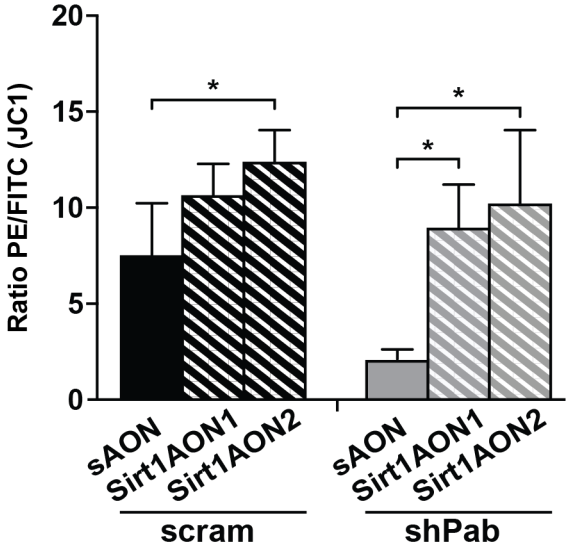

Bar charts shows the mitochondrial membrane potential (ratio of PE/FITC) in scram and shPab cell cultures. The scrambled AON treated cultures are depicted in the solid bars and the *Sirt1*-AON treated in dashed bars. Averages and standard variations are from N=3 biological replicates. Statistical difference was assessed with the Student's t-test, $p<0.05$ is depicted with an asterisk.

Figure S8. Knock down of SIRT1 in muscle cell culture. Related to Fig. 6.

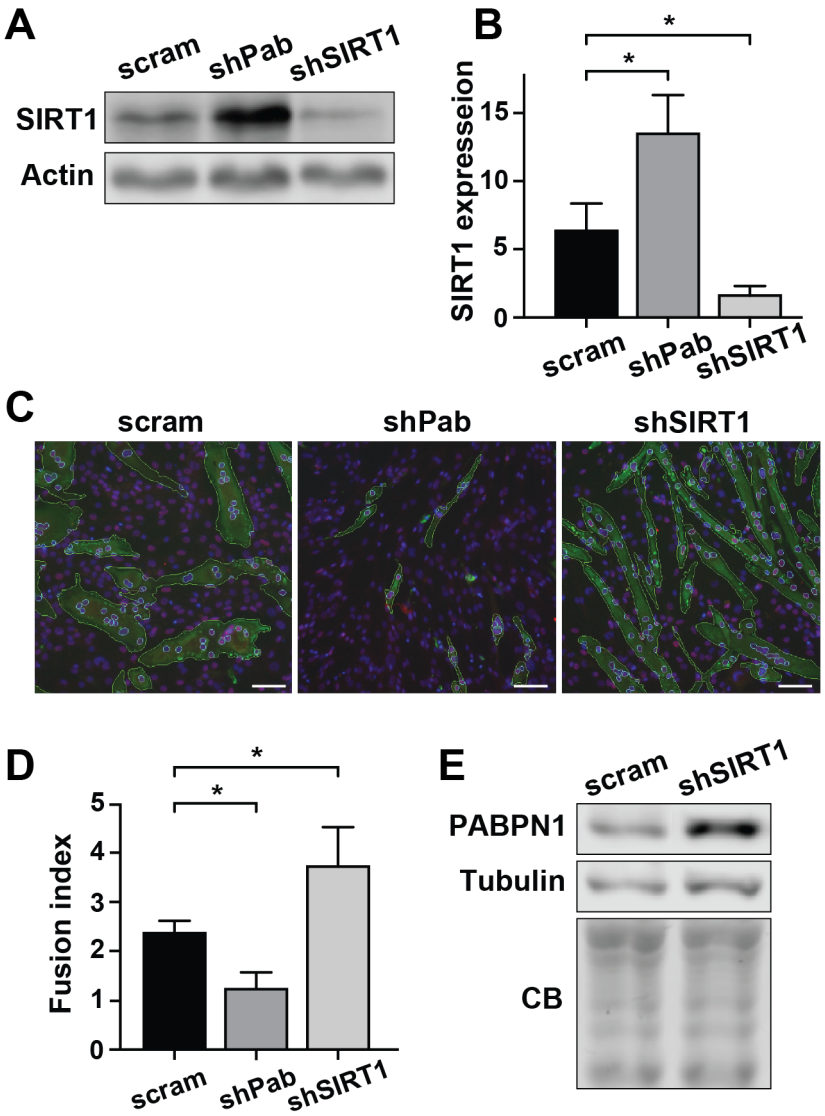

A. Representative western blot of SIRT1 in shPab and shSIRT1 compared to scram muscle cell culture. Actin is used as loading control. **B.** Bar chart show quantification of SIRT1 expression in muscle cell culture. **C.** Representative images show fused C2C12 cells of scram, shPab and shSIR1 cultures. The fused cells are depicted in green and the nuclei are depicted in purple. Scale bar is 20 µm. **D.** Bar chart shows the fusion index of the fused cell cultures. **E.** Western blot of PABPN1 in shSIRT1 muscle cell culture. Tubulin and Coomassie blue (CB) were used as loading controls. Averages and standard variations in this figure are from N=3, additionally, the fusion index was calculated from ~10,000 cells per condition. Averages and standard variations are from N=3 biological replicates. Statistical difference was assessed with the Student's t-test, $p<0.05$ is depicted with an asterisk.

Figure S9. Sirtinol treatment leads to higher PABPN1 accumulation in human muscle cell culture. Related to Fig. 6.

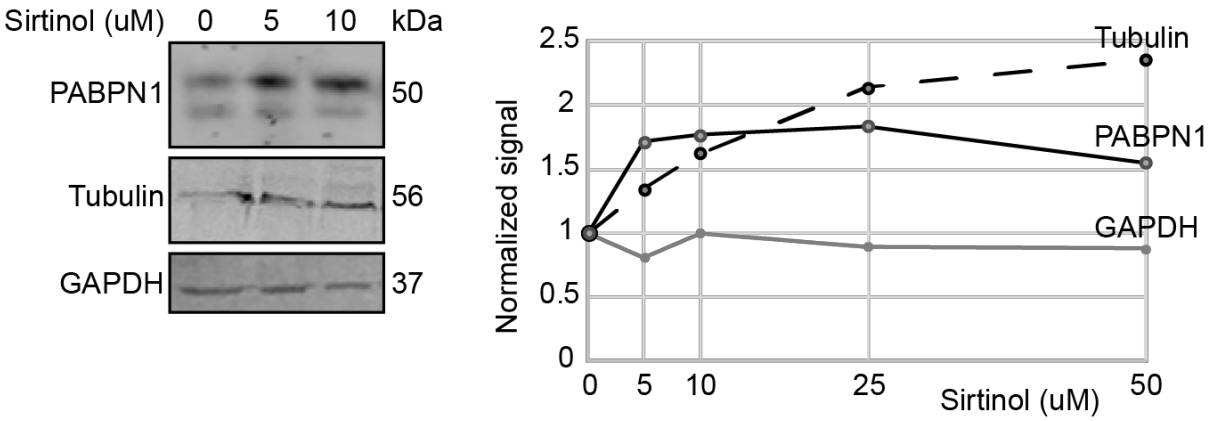

Unmanipulated human muscle cell culture were treated with increasing Sirtinol concentration (0-50uM) for 16 hours. PABPN1, Tubulin and GAPDH protein accumulation were determined using western blots. Plot shows quantification of the signal after normalization to mock (0) treatment.

Figure S10. Reduced PABPN1 levels lead to Myosin heavy chain type 2B foci formation. Related to Fig. 7.

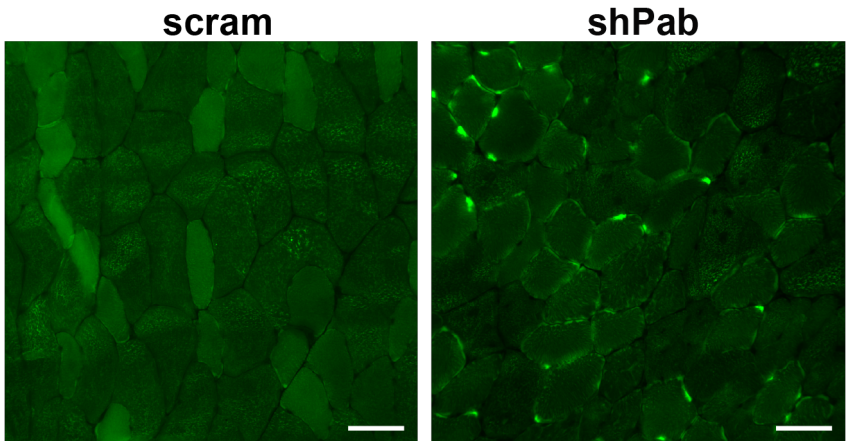

Representative images of MyHC-2B staining in scram and shPab muscle cross-section. shPab muscles clearly show formation of MyHC-2B foci whereas these were completely absent in scram muscles. Scale bar is 50 µm.

Figure S11. RNAseq density plots Related to Fig. 2A and to Methods.

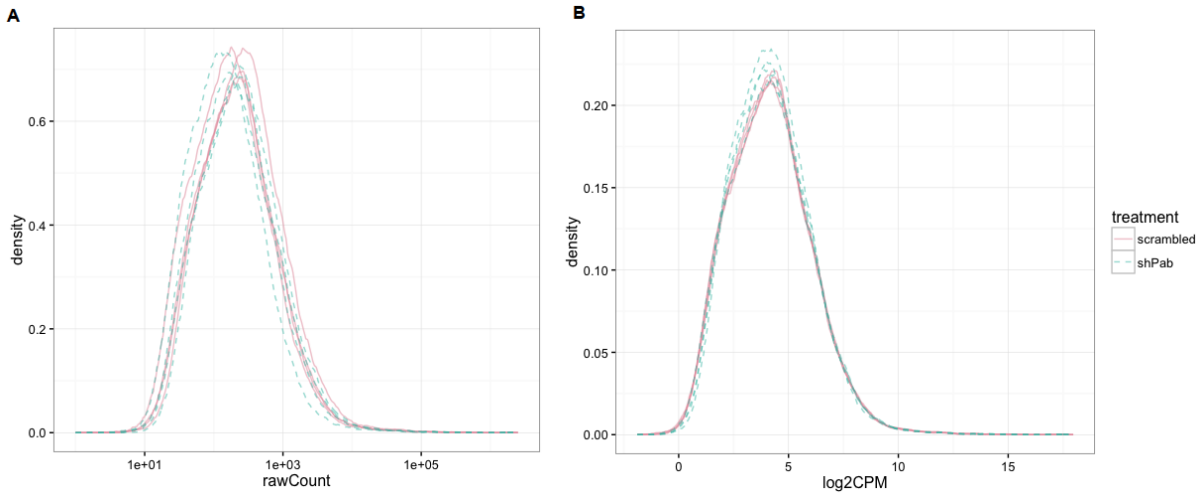

Density plot indicate the sequencing quality of each muscle before (A) and after (B) normalization. The scram muscles are indicated with solid line and the treated muscle with dashed lines.

Figure S12. Proteome distribution plot. Related to Fig. 2B and to Methods.

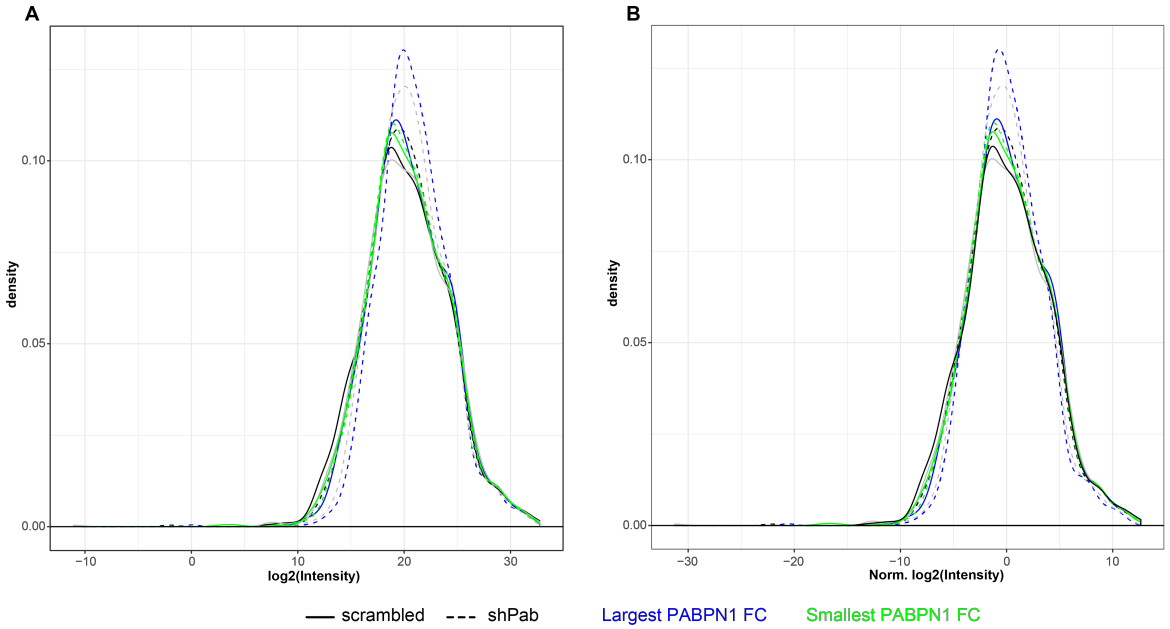

Density plot shows the proteome distribution before (left) and after normalization (right). Solid line indicates the scram muscles whereas dashed lines indicate the shPab muscles. The mouse with the highest difference is depicted in blue and the lowest difference in green.

Figure S13. Acetylome distribution plots. Related to Fig. 4B and to Methods.

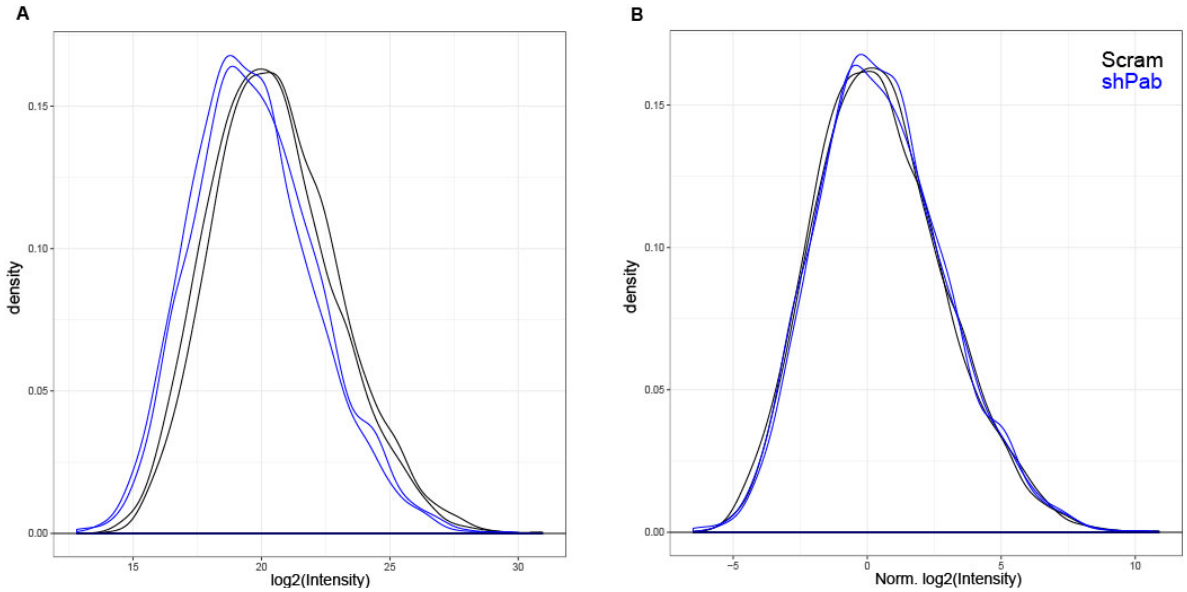

A. distribution plot before normalization. **B.** distribution after normalization.

Density plot shows the acetylome distribution before (left) and after normalization (right). Black line indicates scram and blue the shPab samples.

Transparent Methods

Animal ethics Statement

Animal experiments were conducted according the animal research protocol (DEC # 13113) approved by the animal ethical committee, LUMC, Leiden, the Netherlands, and all experiments were carried out in accordance with the ARRIVE guidelines as previously described (Riaz et al., 2016).

Mouse strain, AAV injection and live mice imaging

PABPN1 was down regulated in mice muscles as previously described (Riaz et al., 2016). In brief, four mice were injected with AAV-based expression cassette containing shRNA to *Pabpn1* and scrambled shRNA (Table S7). AAV9 particles (1.5×10^{12} gc in 50 µl PBS) of *Pabpn1* (shPab) or scrambled (scram) shRNA were contralaterally injected into left or right leg muscles, tibialis anterior. AAV injections, mice house-keeping and muscle harvesting were carried out as detailed in (Riaz et al., 2016), with the exception that in this study muscles were harvested five weeks post-injection for the proteome and transcriptome studies and three weeks post-injection for the acetylome study.

For sirtinol treatment, the aforementioned AAV9-shPab particle dosage was injected into tibialis anterior muscles of both left and right leg of three mice (N=3). AAV9-Scrambled particles were injected into three additional mice as control. Three weeks post AAV injection, the left leg tibialis anterior muscle was injected with sirtinol (0.014 µg/ g muscle mass), and the right leg tibialis anterior muscle was injected with PBS/DMSO (1:1000) vehicle as a control. A second dosage of sirtinol or vehicle was injected after 10 days, and mice were sacrificed after the sixth week of AAV9 injection. Muscles were harvested and stored as described above for subsequent ex-vivo analyses.

Muscle cell culture

Stable knockdowns were generated in immortalized mouse myoblasts C2C12 were generated using a lentivirus transduction containing shRNA to *Pabpn1* as previously described (de Klerk et al., 2012) or shRNA to *Sirt1* (Table S7). Cells were maintained in growth medium (DMEM+10% FCS) containing puromycin (2.5 µg/mL; Sigma-Aldrich). Cell fusion was conducted in DMEM+2% horse-serum for 10 days. Sirtinol (10µM, Sigma Aldrich) treatment was carried out for 24 hours.
AONs to SIRT1 (Table S7) were transfected (1µg) using PEI reagent (Sigma). Scrambled AON FITC-conjugated was used to assess transfection efficiency as described in (Aartsma-Rus et al., 2004). mRNA levels and mitochondrial activity were determined 48 hours post-transfection.

RNA procedures

RNA isolation, library preparation and sequencing RNAseq analysis

Total RNA from scram and shPab muscles of all four mice was isolated using Qiagen miRNeasy Mini kit (Qiagen BV, Venlo, The Netherlands), as described in (Riaz et al., 2016). The quality of bulk RNA including small RNA was determined using bioanalyzer (Agilent Technologies, Santa Clara, CA, USA). cDNA library for RNAseq was prepared from 500ng RNA using oligo-dT Dynabeads (LifeTech 61002)(Parkhomchuk et al., 2009). The NEB Next generation sequencing kit was used to prepare the samples for strand-specific sequencing without a size selection step, according to the manufacturer instructions with following modifications: the library was treated with USER enzyme (NEB M5505L, New England BioLabs Inc, Ipswich, MA, USA) to digest fragments derived from the second strand. After amplification of the libraries, samples with unique sample indexes were pooled and subjected to paired-end 2x100 base pair sequencing on one Illumina-HiSeq2000-v3 lane as per manufacturer instructions (Illumina HQ San Diego CA, USA). Analyses and base calling were carried out by the Illumina pipeline (Illumina HQ San Diego CA, USA). The paired end raw reads were aligned to the GRCm38/mm10 mouse reference genome using the GENTRAP (Generic Transcriptome Analysis Pipeline, March 2015, developed by SASC, https://git.lumc.nl/rig-framework/gentrap) pipeline. Strand specific alignment was carried out with GSNAP version 2013-10-12 using default settings except for novel splicing (=1). UCSC Ensembl transcripts (downloaded on July 17, 2014) were used to identify coding regions (CDS) annotations. Cufflinks v.2.1.1 strict mode was used for quantification of reads at gene and transcript levels. RNAseq QC features are found in Table S8. Normalization was carried out

using the trimmed mean of M values (TMM)(Robinson and Oshlack, 2010). The effect of TMM normalization on reads' distribution is shown in Fig. S11. Raw counts were normalized in EdgeR version 3.14.0 using TMM, and differential expression was determined after fitting a generalized linear model with two fixed effects, donor (mouse) and type (muscle type), using the glmFit function and using tag-wise dispersion estimates. Low quality reads and adaptor sequences (<1%) were filtered out. On average over 10 million reads per sample were mapped to gene exon regions and were counted in further analysis. We did not find significant differences in quality control sequencing features between scram and shPab muscle samples (Table S8 and Fig. S11). Differential expression was identified with the DiffExpr2, an in-house developed pipeline, using a paired log-ratio likelihood (LRT) on gene level.

Quantitative RT-PCR

Total RNA was isolated from cell cultures using Nucleospin kit, Macherey-Nagel. Complementary DNA synthesis was carried out using the RevertAid First Strand cDNA Synthesis Kit (Thermo Fisher Scientific). 3 ng cDNA was used as template per PCR reaction with specific primers (Table S9). qRT-PCR was carried out using LightCycler 480 System (Roche Diagnostics). All qRT-PCR from cell culture were run in biological triplicates and technical duplicates. The qRT-PCR runs from the muscles of all four mice have been done in technical triplicates. Expression levels were calculated after normalization to *Hprt* housekeeping gene. A change in PAS utilization was calculated by the ratio of PCR products between distal to proximal primer sets.

Protein procedures

Protein extraction from muscles

To minimize biological variations, parts of the same muscles that were used for histology and RNA analyses were used for protein analysis. 20 mg muscle tissue from scram and shPab muscles of all four mice was homogenized in RIPA extraction buffer (50mM Tris, pH 7.4, 150mM NaCl, 1% SDS, 0.5% sodium deoxycholate, 1% Igepal CA-630 and protease inhibitors cocktail (Sigma-Aldrich) with plastic beads using bead beater (Precellys Stretton Scientific). The muscle extract was subsequently sonicated on ice (3x 5 seconds, 15W). Protein concentrations were determined with a BCA protein assay kit (Pierce, Thermo Fisher Scientific). For the acetylome, proteins were extracted using 9M urea buffer (20mM HEPES pH 8.0, 9M urea, 1mM sodium orthovanadate, 2.5mM sodium pyrophosphate, 1mM β-glycerophosphate). Scrambled shRNA injected muscles from seven mice were pooled together as control and the seven PABPN1 shRNA injected muscles were pooled together for the acetylated peptide pull-down.

Mass spectrometry sample preparation

Peptides were obtained by a tryptic digestion according to the filter-aided sample preparation method as previously described (Wisniewski et al., 2009). In brief, 50µg protein was pre-treated with DTT (20mM), IAA (1M) and washed with urea (8M) in between. Protein digestion was carried out with 1.7µg trypsin per muscle at 37ºC overnight. Trypsin was deactivated with 5% formic acid and the peptides were then washed with NaCl (0.5M) and H_2O. Subsequently, peptide desalting was performed using C18 Sep-Pack cartridges (Waters), and dried using miVac DUO concentrator (Genevac, UK). Peptides were stored in -20°C.

For the acetylome peptides were pulled down using PTMScan Acetyl-Lysine [Ac-K] Immunoaffinity Beads (Cat. #14499; CST, Inc) according to the manufacturer protocol (CST, Inc). In brief, 17mg protein was reduced with DTT (4.5mM) at 55°C for 30 min and then alkylated IAA (100mM) in the dark at room temperature for 15 min. The samples were then diluted 4 times using 20mM HEPES pH 8.0. Protein digestion was carried out with 10ug/ml trypsin at RT overnight. Trypsin was deactivated with trifluoroacetic acid (TFA). Peptides were kept at -80°C and subsequently lyophilized for 48 hours to ensure complete removal of TFA. The peptide pellet was resuspended in Immunoaffinity Purification buffer (IAP) (50mM morpholinepropanesulfonic acid pH 7.2, 10mM sodium phosphate dibasic, 50mM sodium chloride). Resuspended peptides were directly loaded on the immunoaffinity Beads (Cat. #14499; CST, Inc) and were incubated at 4°C for 2 hours. The beads-peptide complexes were washed with 0.15% TFA after IAP and RODI water. The eluted peptides were subsequently purified using C18 tips, and then dried using miVac DUO concentrator from Genevac, UK.

All peptide samples (proteome and acetylome) were resuspended in 20 µl solution A (98% MilliQ-H_2O, 2% CH_3CN and 0.1% FA), vortexed and sonicated before injection into the Q Executive HF Hybrid Quadrupole-Orbitrap Mass Spectrometer (Thermo Fisher Scientific). Mass spectrometry was run on a one-hour gradient in technical duplicates, essentially as previously described (Fye et al., 2018).

Proteome peptide analysis

The proteome chromatograms were aligned using Progenesis QI software (Nonlinear dynamics, Nonlinear dynamics, Waters, Version 2.0.5556.29015). The peptides were identified using the Mascot (Matrix Science version 2.5.1) search engine and Uniprot mouse database. Carbamidomethylation (C) was set as a fixed, and deamidation (N) and oxidation (M) were set as variable modifications in the MS/MS Ions searches. Protein identification confidence was set up with 1% FDR. The correlation coefficient between technical replicates was close to one for all eight muscles (Table S10), indicating excellent reproducibility. The protein abundances were averaged from the technical replicates and were subsequently normalized by subtraction of the median (Fig. S12). Proteins that were found in at least five muscles out of eight were included in further analyses (N=1213) (Table S3).

Acetylome peptide analysis

The acetylome chromatograms were aligned and peptides were identified using PEAKS Studio 8.0 software (Bioinformatics Solutions Inc. (BSI), Version 8, build 20160908) and were mapped using Uniprot mouse database. In addition to the modifications set for the shPab proteome, peptides acetylation (K) and carbamylation (K) were set as variable modifications in the MS/MS Ions searches for the precipitated peptides. 1% FDR and a mass error tolerance of 10.0 ppm and a retention time shift tolerance of 5 minutes were allowed in the peptide quantification. Peptide intensities were normalized by subtraction of the median (Fig. S13). The peptides were next selected for confidence based on the following criteria: measurement in all four runs, or peptides that were found in only one muscle group (scram or shPab), subsequently the Coefficient of Variation (CV) was used to assess technical reproducibility. A CV-cutoff was determined from the peptide measurement quality (MS1-channel), and the average was calculated from the two muscle groups. A cutoff of CV<0.3 was used for peptide selection. The differentially acetylated peptides were considered with a CV<0.3 and fold change >|1.5|.

Proteomics data availability

The mass spectrometry proteomics data have been deposited to the Proteome X change Consortium via the PRIDE (Perez-Riverol et al., 2016) partner repository. The shPab proteome with the dataset identifier PXD004865 and 10.6019/PXD004865 and the shPab acetylome with the dataset identifier PXD011534 and 10.6019/PXD011534.

Western blot analyses

30µg aliquots of protein extracts were separated on SDS-PAGE (Criterion XT, Bio-Rad). Western blot was carried out using PVDF membranes. Antibodies used in this study are listed in Table S8. Fluorescent signals were detected using the Odyssey CLx Infrared imaging system (LiCOR, NE. USA). Quantification of protein accumulation was performed with ImageJ version 1.48 (https://imagej.nih.gov/ij/). Values were corrected for background and normalized to loading controls.

Histology, immunofluorescence and imaging

Cryosectioning, histology and immunofluorescence was carried out as described in (Riaz et al., 2016). All imaging analyses were calculated from 5 frames covering the entire cross section. Cryosections were stained with Gomori-Trichrome staining (Gomori, 1950) Cell-based imaging and subsequent quantification was carried out using Arrayscan VTI HCA, Cellomics (Thermo Fisher Scientific). Myotubes were visualized using antibody to myosin heavy chain (MF20) and mitochondrial membrane potential was assessed with JC1 dye (Thermofisher Scientific) as described in (Anvar et al., 2013). Other antibodies that were used in immunofluorescence are listed in Table S8.

Statistics and bioinformatics

P-values between shPab and scram AAV injections, or vehicle and sirtinol treated muscles were carried out using the parametric paired *t*est. The paired test overcomes inter-individual variations. The

parametric t-test was applied after assessment of dataset normality (proteome, transcriptome, and acetylome (Figures S11-S13), and comparing mean to median, and kurtosis and skewness values. Since the proteome and transcriptome datasets showed normal distribution, statistical assessment of the in vitro experiments was carried out with the parametric paired test. P-values for RNAseq were corrected for multiple testing using Benjamini and Hochberg's FDR. A fold change correlation between the overlapping genes and proteins was assessed using the Spearman Rank test. Statistical analyses of validation studies were carried out with the parametric paired test in R and in Graphpad Prism version 6.0. Enrichment in functional groups was carried out DAVID v6.7 (https://david.ncifcrf.gov/). Protein-protein interaction networks were created in STRING (https://string-db.org/; v10.5).

A detailed explanation for the choice of paired t-test: the power

What is the power gain of the paired t-test compared to the unpaired? The way to answer this question is to assume that we have paired data (otherwise we cannot do a paired t-test). We will compare the regular paired analysis that we would normally do with the unpaired analysis that we would do if we had accidentally thrown away the pairing information.

Consider the following model. Let the 'before' measurment in pair i be $X_i = P_i + E_i$ and the 'after' measurement be $Y_i = P_i + F_i$. We assume $E_i \sim N(0, \sigma^2)$, $F_i \sim N(0, \sigma^2)$, $P_i \simeq N(0, \tau^2)$, all independent.

The mean $D = X - Y = X - Y$ is the same in both analyses. The estimated variance is difference, however. In the unpaired analysis, $X_i - Y_i$ has variance $2\sigma^2$, so D has variance $2\sigma^2/n$. In the unpaired analysis X_i has variance $\sigma^2 + \tau^2$ and so has Y_i. In the unpaired analysis we ignore the correlation, so we will say that D has variance $(2\sigma^2 + 2\tau^2)/n$.

We can ask what n gives the same power. If n_p is the sample size of the paired analysis and n_u of the unpaired, we have approximately the same power if the variances are about the same, so if

$$\frac{2\sigma^2 + 2\tau^2}{n_u} = \frac{2\sigma^2}{n_p},$$

equivalently if

$$\frac{n_p}{n_u} = \frac{\sigma^2}{\sigma^2 + \tau^2}.$$

The fraction of sample size gained in the paired analysis is

$$\frac{n_u - n_p}{n_u} = \frac{\tau^2}{\sigma^2 + \tau^2}.$$

The right-hand side is the fraction of the variance in the data explained by the pairing. Caveat: the paired test has an advantage because it uses a larger number of degrees of freedom in the t-distribution. The paired test has therefore a small advantage if the sample size is small.

Supplemental References

Aartsma-Rus, A., Kaman, W.E., Bremmer-Bout, M., Janson, A.A., den Dunnen, J.T., van Ommen, G.J., and van Deutekom, J.C. (2004). Comparative analysis of antisense oligonucleotide analogs for targeted DMD exon 46 skipping in muscle cells. Gene Ther *11*, 1391-1398.
Anvar, S.Y., Raz, Y., Verway, N., van der Sluijs, B., Venema, A., Goeman, J.J., Vissing, J., van der Maarel, S.M., t Hoen, P.A., van Engelen, B.G.*, et al.* (2013). A decline in PABPN1 induces progressive muscle weakness in oculopharyngeal muscle dystrophy and in muscle aging. Aging (Albany NY) *5*, 412-426.
de Klerk, E., Venema, A., Anvar, S.Y., Goeman, J.J., Hu, O., Trollet, C., Dickson, G., den Dunnen, J.T., van der Maarel, S.M., Raz, V.*, et al.* (2012). Poly(A) binding protein nuclear 1 levels affect alternative polyadenylation. Nucleic Acids Research *40*, 9089-9101.
Fye, H.K.S., Mrosso, P., Bruce, L., Thézénas, M.-L., Davis, S., Fischer, R., Rwegasira, G.L., Makani, J., and Kessler, B.M. (2018). A robust mass spectrometry method for rapid profiling of erythrocyte ghost membrane proteomes. Clinical Proteomics *15*, 14.
Gomori, G. (1950). A rapid one-step trichrome stain. American journal of clinical pathology *20*, 661-664.
Parkhomchuk, D., Borodina, T., Amstislavskiy, V., Banaru, M., Hallen, L., Krobitsch, S., Lehrach, H., and Soldatov, A. (2009). Transcriptome analysis by strand-specific sequencing of complementary DNA. Nucleic Acids Res *37*, e123.
Perez-Riverol, Y., Xu, Q.W., Wang, R., Uszkoreit, J., Griss, J., Sanchez, A., Reisinger, F., Csordas, A., Ternent, T., Del-Toro, N.*, et al.* (2016). PRIDE Inspector Toolsuite: Moving Toward a Universal Visualization Tool for Proteomics Data Standard Formats and Quality Assessment of ProteomeXchange Datasets. Molecular & cellular proteomics : MCP *15*, 305-317.
Riaz, M., Raz, Y., van Putten, M., Paniagua-Soriano, G., Krom, Y.D., Florea, B.I., and Raz, V. (2016). PABPN1-Dependent mRNA Processing Induces Muscle Wasting. PLoS Genet *12*, e1006031.
Robinson, M.D., and Oshlack, A. (2010). A scaling normalization method for differential expression analysis of RNA-seq data. Genome Biology *11*, R25-R25.
Wisniewski, J.R., Zougman, A., Nagaraj, N., and Mann, M. (2009). Universal sample preparation method for proteome analysis. Nat Meth *6*, 359-362.